

# A prenatal window for enhancing spatial resolution of cortical barrel maps

Received: 24 June 2024

Accepted: 5 February 2025

Published online: 06 March 2025



Mar Anibal-Martínez<sup>1</sup>, Lorenzo Puche-Aroca<sup>1</sup>, Elena Pérez-Montoyo<sup>1</sup>, Gabriele Pumo<sup>2,3</sup>, M. Pilar Madrigal<sup>4</sup>, Luis M. Rodríguez-Malmierca<sup>1</sup>, Francisco J. Martini<sup>1</sup>, Filippo M. Rijli<sup>2,3</sup> & Guillermina López-Bendito<sup>1</sup>✉

Precise mapping of peripheral inputs onto cortical areas is essential for accurate sensory processing. In the mouse primary somatosensory cortex, mystacial whiskers correspond to large, well-defined barrels, while upper lip whiskers form smaller, less distinct barrels. These differences are traditionally attributed to variations in whisker input type and receptor density, but prenatal activity and transcriptional programs also impact somatosensory map development independently of sensory experience. Here, we demonstrate that prenatal ablation of mystacial whiskers leads to a remapping of cortical territories, enhancing the functional and anatomical definition of upper lip whisker barrels. This reorganization occurs without altering peripheral receptor types. Instead, thalamic neurons that receive upper lip inputs adopt a mystacial-like transcriptional profile. Our findings unveil a regulated prenatal mechanism in the thalamus that ensures sufficient cortical barrel size and spatial resolution for sensory processing, irrespective of peripheral receptor type or density, highlighting a critical developmental process in sensory mapping.

Sensory systems are represented in the primary sensory areas of the brain, structured into both anatomical and functional maps<sup>1–4</sup>. The spatial precision of sensory maps varies among species according to the ethological relevance of the modality or the intra-modal sensory branch<sup>5</sup>. This precision is achieved through the accuracy of point-to-point innervation along the ascending sensory pathway. In rodents, which heavily rely on the somatosensory modality, a prominent cortical area is devoted to processing stimuli from facial whiskers. Within the mouse primary somatosensory cortex (S1), information from facial whiskers is processed in two juxtaposed subfields: the posteromedial barrel subfield (PMBSF) and the antero-lateral barrel subfield (ALBSF). The PMBSF receives input from the mystacial whiskers which provide diverse and specialized information to S1<sup>6,7</sup>. The ALBSF receives input from the upper lip whiskers which are considered to play a secondary role in sensory processing<sup>8</sup>. While each barrel corresponds to a single whisker in both regions, the degree of clustering of incoming

thalamocortical axons varies, leading to notable anatomical distinctions between the two territories. While PMBSF barrels are characterized by their large size and sharp borders, ALBSF barrels are smaller and have poorly defined borders<sup>9</sup>. These differences in intra-modal map organization parallel the distinct morphological characteristics of mystacial and upper lip whiskers: mystacial whiskers are long with large follicles, whereas upper lip whiskers are comparatively short with small follicles, albeit more abundant. Despite their clear anatomical and functional differences, we still lack a complete understanding of the mechanism underlying the construction of these two distinct barrel maps and to what extent they rely on the type of sensory receptors (mystacial versus upper lip). Indeed, recent data demonstrated that sensory receptor-independent mechanisms can also influence cortical barrel size by altering the patterns of activity in subcortical stations. For instance, increasing thalamic waves in the developing somatosensory thalamus of early blind mice results in

<sup>1</sup>Instituto de Neurociencias de Alicante, Universidad Miguel Hernández-Consejo Superior de Investigaciones Científicas (UMH-CSIC), San Juan de Alicante, Alicante, Spain. <sup>2</sup>Friedrich Miescher Institute for Biomedical Research, Fabrikstrasse 24, 4056 Basel, Switzerland. <sup>3</sup>University of Basel, Basel, Switzerland.

<sup>4</sup>Departamento de Histología y Anatomía, Facultad de Medicina, Universidad Miguel Hernández (UMH), San Juan de Alicante, Alicante, Spain.

✉ e-mail: [g.lbendito@umh.es](mailto:g.lbendito@umh.es)

larger barrels in the PMBSF of S1, even before the onset of active whisking<sup>10,11</sup>. Thus, the size of a sensory barrel map may not only depend on the type and number of sensory receptors but may also be regulated by intrinsic programs during development. By embryonically ablating mystacial whiskers and follicles, and the subsequent PMBSF representation, we generated mice in which the ALBSF barrels become larger and better-defined, without altering the size and number of upper lip follicles. This intra-modal reorganization of the barrel maps occurs within a restricted prenatal time window and is guided by transcriptional programs operating intra-modally in the thalamus. Interestingly, these reorganized ALBSF barrels resemble normal PMBSF barrels at the morphological, molecular, and functional levels, showing an enhanced spatial resolution upon tactile stimulation.

## Results

### The size of barrel subfield areas can be adjusted prenatally

The size of the areas devoted to processing distinct whisker-mystacial versus upper lip input information is thought to be determined by the corresponding type and density of sensory receptors on the mouse face<sup>12,13</sup>. We asked whether prenatal removal of a selected facial whisker type might have an impact on the cortical barrel areas and spatial distribution of the spared whiskers. We implemented a strategy whereby the mystacial whiskers in the whisker pad were cauterized unilaterally at embryonic day (E) 14 (named as embWPC), in both wildtype and TCA-GFP mice<sup>14</sup>, in which thalamocortical projections are labeled with green fluorescent protein (GFP). At this stage, trigeminal nerve axons have just begun to target the principal trigeminal sensory nucleus (PrV) in the brainstem (Supplementary Fig. 1a), but PrV neuron axons have not yet entered the ventral posteromedial (VPM) thalamic nucleus<sup>15–19</sup>.

Analysis of the snout at E18 confirmed the specific ablation of the mystacial whiskers and follicles (Fig. 1a, b), with a strong reduction of whisker pad-innervating primary trigeminal sensory axons targeting the PrV (Supplementary Fig. 1b). At early postnatal stages, the total areas of PrV, thalamic ventral posterior nucleus (VPN) and S1, including other somatosensory body representations apart from the snout, did not exhibit significant differences in embWPC, as compared to control mice (Supplementary Fig. 2a–h). In contrast, the size of the areas corresponding to mystacial and upper lip whiskers was significantly rescaled in embWPC mice at all levels of the pathway, suggesting intra-modal plasticity of connectivity. For example, in S1, we found a 54% decrease in the PMBSF territory, and a 34% expansion of the ALBSF territory, a phenomenon already observed in P4 (Fig. 1c, d and Supplementary Fig. 2i, j). Notably, we found no discernible differences in the total upper lip volume, nor in the volume and number of upper lip follicles between control and embWPC mice both at E18 and P8 (Fig. 1a, b and Supplementary Movies 1, 2). Dye depositions in the cortical PMBSF or ALBSF of P8 embWPC confirmed a similar intra-modal remapping of the corresponding whisker pad input-receiving VPM (wpVPM) or upper lip input-receiving VPM (ulVPM) areas in the thalamic VPM<sup>20</sup> (Fig. 1e, f). Moreover, retrogradely labeled thalamocortical neurons within each VPM sub-territory maintained their expected point-to-point distribution, matching cortical topography (Supplementary Fig. 3).

Importantly, the changes of the cortical barrel field sub-territories depended on mechanisms only present before birth, since cauterization of the whisker pad at postnatal day 0 (P0), referred to as POWPC, revealed no significant territorial differences in the PMBSF and ALBSF between control and POWPC across the somatosensory stations (Fig. 1g, h and Supplementary Fig. 4). As expected, there were no rearrangements of the thalamocortical axons in the POWPC (Fig. 1i, j and Supplementary Fig. 5). Notably, barrels in PMBSF exhibited a diminished degree of definition and structure, with blurred point-to-point topography, highlighting the enduring effects of early sensory deprivation on the cortical organization (Supplementary Fig. 5c, d). Thus,

there is a critical window in which the cortical ALBSF area can be significantly adjusted without altering upper lip receptors, suggesting that after this timepoint, plasticity might arise from a different strategy to compensate for sensory loss.

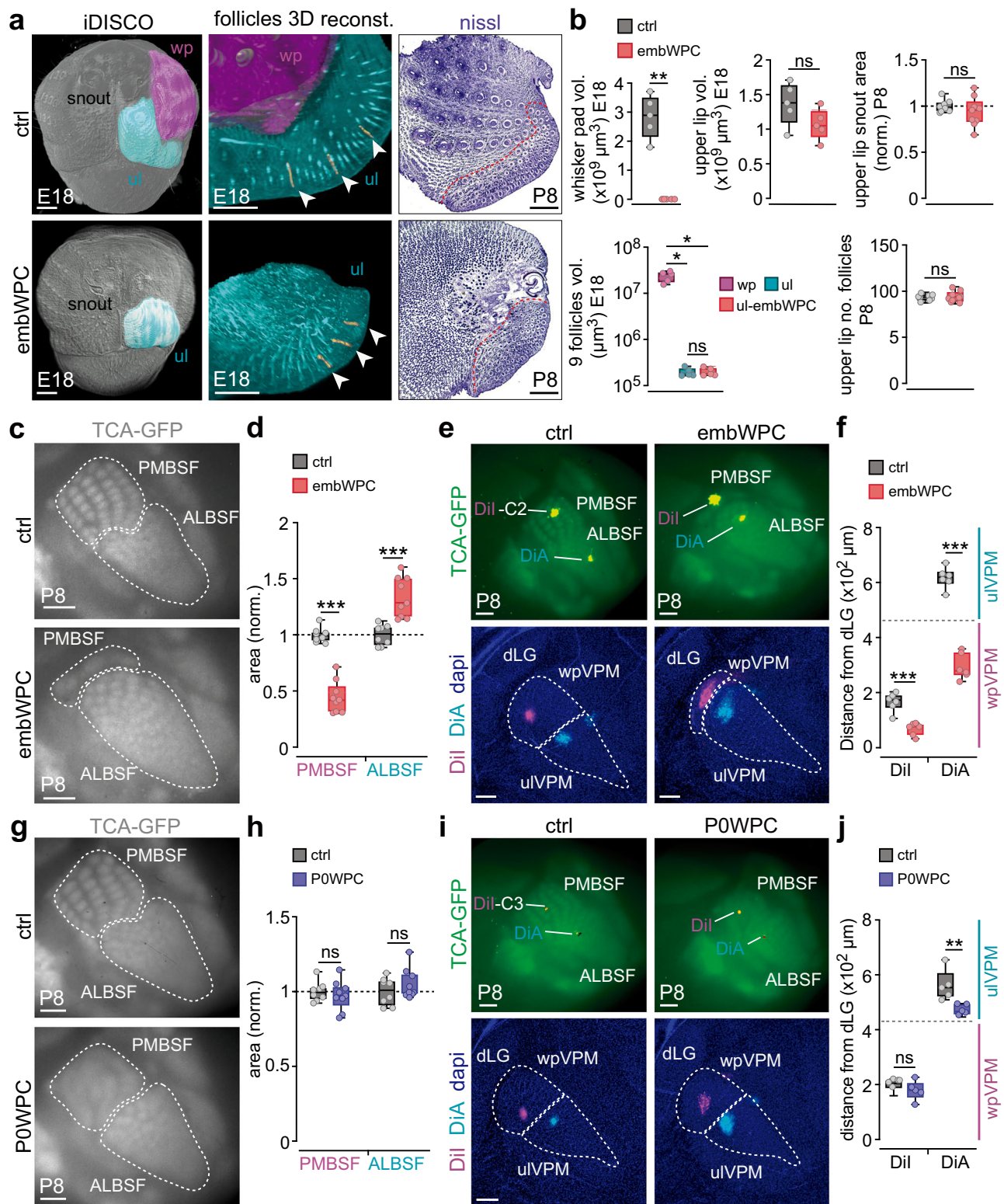
### Functional rescaling of ALBSF in embWPC mice occurs before birth

Whisker pad stimulation *in vivo* at E18 can elicit activity in the developing PMBSF<sup>21,22</sup>, indicating that the periphery-to-cortex somatosensory pathway is already functional before birth. We asked whether the anatomical changes observed in embWPC at P8 were detectable at prenatal stages by assessing functional reorganizations. We carried out peripheral whisker pad and upper lip stimulations at E18 while recording cortical calcium activity in *Emx1*<sup>GCaMP6f</sup> transgenic mice, expressing GCaMP6f in cortical glutamatergic neurons<sup>22</sup> and carrying unilateral whisker pad cauterization (Fig. 2a). We also used non cauterized mice as additional controls.

Stimulations of either the whisker pad or the upper lip in control mice or in the control side of embWPC mice at E18 elicited responses from clusters of cortical neurons corresponding to the putative territories of the PMBSF or ALBSF, respectively (Fig. 2b, c, Supplementary Fig. 6, and Supplementary Movie 3). In contrast, whisker pad stimulations in the cauterized side of embWPC mice triggered very reduced responses in the caudal-most part of the expected contralateral PMBSF (“PMBSF”), confirming the anatomical reduction of this territory. Remarkably, stimulations of the upper lip in the cauterized side elicited misplaced responses in the expected ALBSF (“ALBSF”) that notably expanded into the “PMBSF” (Fig. 2b, c and Supplementary Movie 4), as compared to the control side. This ectopic “PMBSF” activation was maintained at P4 when the size of responses to upper lip stimulation were already refined in the control side (Fig. 2d–g and Supplementary Movies 5, 6). Thus, the anatomical rescaling of barrel field sub-territories seen in the postnatal embWPC can be functionally detected prior to birth.

### Silencing prenatal thalamic synchronous activity does not prevent the area rescaling of barrel subfields

Thalamic neurons display waves of prenatal spontaneous activity that are crucial for the development of cortical barrel field maps<sup>10,21</sup>. Therefore, we investigated whether the rescaling of barrel field territories in embWPC embryos could be explained by changes in the spontaneous activity of VPM neurons. Inputs from the whisker pad at E16 are carried by afferents from the ventral portion of the PrV (vPrV), whereas inputs from the upper lip are carried by afferents from dorsal PrV (dPrV)<sup>17–19</sup>. While at this prenatal stage, vPrV afferents topographically target the dorsolateral VPM (the prospective wpVPM), dPrV afferents target not only the ventromedial part (the prospective ulVPM) but cover most parts of the VPM<sup>17,19</sup>. Thus, while whisker pad and upper lip inputs are segregated at the brainstem nuclei, dPrV and vPrV axon terminals prenatally overlap within the prospective wpVPM territory<sup>17,19</sup> (Fig. 3a, b and Supplementary Fig. 7a–c). Remarkably, despite this axonal overlap, spontaneous activity patterns in the VPM thalamus at E16 were sub-territory specific. We detected a notable distinction in the frequency of spontaneous activity waves between the prospective wpVPM and ulVPM regions. While wpVPM exhibited a high frequency of waves, the prospective ulVPM showed significantly reduced frequency (Fig. 3c, d and Supplementary Movie 7). In embWPC, we observed a striking change in the spontaneous activity pattern, with a significant increase in thalamic wave frequency within the prospective ulVPM, resembling the pattern observed in the control wpVPM primordium (Fig. 3c, d and Supplementary Movie 8). Interestingly, in embWPC VPM at P4, dPrV axon projections did not undergo normal developmental segregation but still targeted most of the dorsolateral VPM, unlike in controls, and covered the area normally occupied by vPrV input afferents (Supplementary Fig. 7d, e).



Thus, during prenatal development whisker input deprivation remaps spontaneous neuronal activity patterns in the future uIVPM territory.

Next, we asked whether the embryonic increased activity in the prospective uIVPM might influence the functional and anatomical rescaling of the ALBSF territory. Thus, we tested this possibility and conducted embryonic whisker pad cauterization in a mouse in which the synchronous spontaneous activity of the thalamus is embryonically

disrupted (referred to as *embWPC-Th<sup>Kir</sup>*)<sup>21</sup>. Briefly, we used a tamoxifen-dependent *Gbx2<sup>CreERT2</sup>* mouse with a floxed line expressing the inward rectifier potassium channel 2.1 (*Kcnj2*) fused to the mCherry reporter in thalamic neurons (referred to as *Th<sup>Kir</sup>*). Our data revealed that thalamic and cortical territories in *embWPC-Th<sup>Kir</sup>* mice exhibited a spatial reorganization similar to that observed in *embWPC* mice. In both mice, the wpVPM and PMBSF territories virtually disappeared, and the uIVPM and ALBSF expanded as compared to the control (Fig. 3e). Consistent with



**Fig. 1 | Whisker pad deprivation in embryos rescues barrel field areas and thalamocortical circuits.** **a** Left and middle, iDISCO frontal snout views showing the whisker pad (magenta) and upper lip (cyan) areas, lateral 3D-reconstructions of the follicles (yellow) at E18. Right, Nissl stainings of the snout at P8, red dashed line delimits upper lip area. **b** Quantification (iDISCO E18,  $n = 5$  ctrl,  $n = 5$  embWPC, Nissl P8,  $n = 8$  ctrl,  $n = 9$  embWPC). **c** Surface view of thalamocortical terminals (TCA-GFP+) in the PMBSF and ALBSF at P8. **d** Quantification ( $n = 8$  ctrl,  $n = 9$  embWPC). **e** Upper panels, Dil and DiA crystal placements in the C2 PMBSF and in the ALBSF, respectively, at P8. Lower panels, backlabelled cells in the wpVPM and ulVPM. **f** Quantification of the position of backlabelled cells with respect to the distance to the dLG nucleus. The gray horizontal dashed line represents the separation between wpVPM and ulVPM ( $n = 6$  ctrl,  $n = 6$  embWPC). **g** Surface view of TCA-GFP+ in the PMBSF and ALBSF at P8. **h** Quantification of the data ( $n = 8$  ctrl,

$n = 9$  POWPC). **i** Upper panels, Dil and DiA crystal placements in the C3 PMBSF and in the ALBSF, respectively, at P8. Lower panels, backlabelled cells in the wpVPM and ulVPM. **j** Quantification of the position of backlabelled cells with respect to the distance to the dLG nucleus. The gray horizontal dashed line represents the separation between wpVPM and ulVPM ( $n = 5$  ctrl,  $n = 5$  POWPC). Source data are provided as a Source data file. wp whisker pad, ul upper lip, E embryonic, P postnatal, embWPC embryonic whisker pad cauterized, POWPC postnatal day 0 whisker pad cauterized, vol. volume, no. number, TCA-GFP thalamocortical axons labeled with a green fluorescent protein, norm. normalized. Scale bars: **a** (left), **c**, **e** (top), **g**, **i** (top) 500  $\mu\text{m}$ ; **a** (middle) 400  $\mu\text{m}$ ; **a** (right) 1000  $\mu\text{m}$ ; **e** (bottom), and **i** (bottom) 200  $\mu\text{m}$ . Boxplots show the medians with the interquartile range (box) and range (whiskers). Bar graphs show the means  $\pm$  SEM. ns not significant. \* $p < 0.05$ , \*\* $p < 0.01$ , \*\*\* $p < 0.001$ .

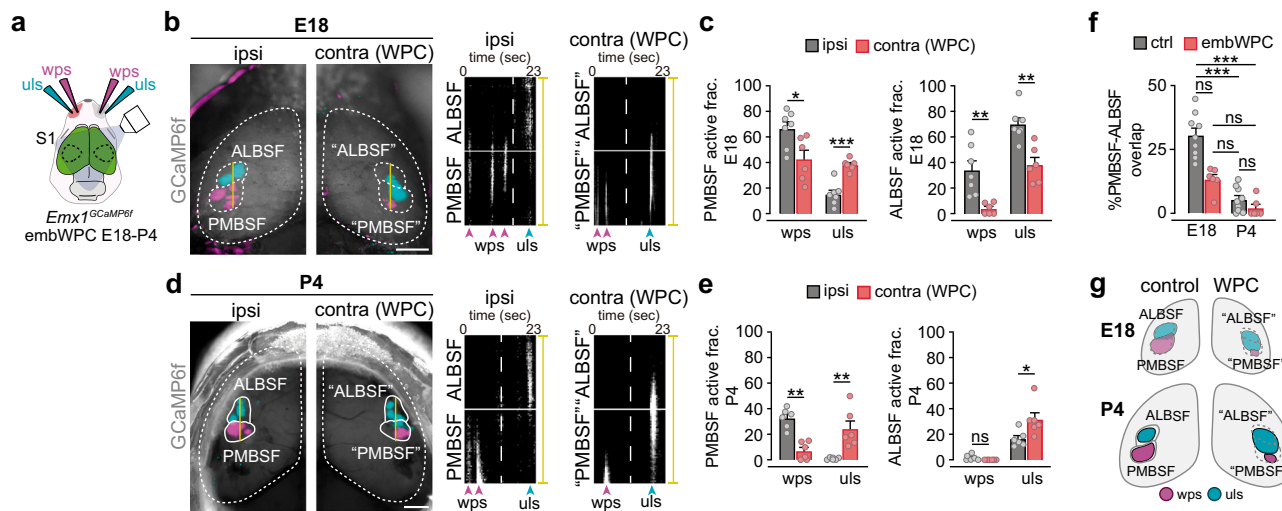


**Fig. 2 | Functional rescaling of cortical barrel field territories in embWPC mice.**

**a** Schema representing the experimental paradigm. **b** Left, cortical evoked responses (GCaMP6f) to whisker pad (magenta) and upper lip (cyan) stimulations in control (ipsilateral) and whisker pad cauterized (WPC, contralateral) sides in embWPC mice at E18. Control PMBSF and ALBSF territories were translated to the WPC side for direct comparison and labeled as "PMBSF" and "ALBSF". Right, reslice of the yellow line in the left, representing responses elicited in PMBSF and ALBSF primordia by whisker pad stimulation (wps) or upper lip stimulations (uls). The white horizontal line delineates the boundaries between PMBSF and ALBSF. The vertical dashed line divides the wps from the uls over time. The arrows label the stimulation times for the whisker pad (magenta) and upper lip (cyan). **c** Quantification of the PMBSF and ALBSF active fraction to wps or uls ( $n = 7$  ctrl,  $n = 6$  WPC). **d** Left, cortical evoked responses (GCaMP6f) to whisker pad (magenta) and upper lip (cyan) stimulations in control (ipsilateral) and WPC (contralateral)

sides in embWPC at P4. Right, reslice of the yellow line in the left, representing responses elicited in PMBSF or ALBSF by wps or uls. The white horizontal line delineates the boundaries between PMBSF and ALBSF. The vertical dashed line divides the wps from the uls over time. The arrows label the stimulation times for the whisker pad (magenta) and upper lip (cyan). **e** Quantification of the PMBSF and ALBSF active fraction to wps and uls ( $n = 6$  ctrl side,  $n = 6$  WPC side). **f** Quantification of the percentage of overlap responses between the PMBSF and ALBSF territories at E18 and P4 ( $n = 9$  ctrl E18,  $n = 6$  embWPC E18,  $n = 9$  ctrl P4,  $n = 6$  embWPC P4). **g** Schema illustrating the results. Dashed lines delineate PMBSF and ALBSF putative evoked territories at E18. Source data are provided as a Source data file. S1, primary somatosensory cortex; GCaMP6f, calmodulin-based genetically encoded fluorescent calcium indicator 6-fast. Scale bars, 1000  $\mu\text{m}$ . Bar graphs show the means  $\pm$  SEM. ns not significant. \* $p < 0.05$ , \*\* $p < 0.01$ , \*\*\* $p < 0.001$ .

previous studies in the *Th<sup>Kir</sup>* mouse<sup>21</sup>, manipulating thalamic activity patterns in the embWPC mice (embWPC-*Th<sup>Kir</sup>*) resulted in the absence of thalamic waves (Supplementary Fig. 8a, b) and, the complete loss of barrels, evidenced by a total lack of TCA clustering, in both PMBSF and ALBSF territories (Fig. 3e, g). Rescaling of thalamic and cortical territories, along with thalamocortical circuits, was still observed in the embWPC-*Th<sup>Kir</sup>* mouse but was virtually absent in the *Th<sup>Kir</sup>* mouse alone, as shown by anatomical and dye tracing analyses (Fig. 3e–h and Supplementary Fig. 8c–g). In sum, our results demonstrate that the patterns of spontaneous activity in prenatal VPM neurons are dispensable for intra-modal thalamic and cortical sub-territories rescaling to input deprivation.

### Upper lip input-receiving thalamic neurons adopt a similar transcriptional profile to mystacial input-receiving neurons

Cross-modal and intra-modal changes in the transcriptional programs of thalamic neurons have been shown to generate thalamocortical

circuit reorganizations and cortical adaptations, as shown in early blind pups or in mice with an early postnatal ablation of the VPM nucleus<sup>10,23,24</sup>. Therefore, we examined whether the anatomical and functional circuit expansion of the ALBSF in embWPC might be influenced by changes in the transcriptional program of VPM neurons. To assess this, we dissected tissue, at similar distances from the dorsal lateral geniculate (dLG) nucleus, from wpVPM and ulVPM in control and embWPC mice at P0 (Fig. 4a, b) and compared their transcriptional profiles by bulk RNA-sequencing (RNA-seq). Principal component analysis (PCA) revealed that the transcriptomes from wpVPM and ulVPM cells in control mice clustered separately already at P0 (Supplementary Fig. 9a). Differential expression analysis (DEA) further revealed 377 differentially expressed genes (DEGs) enriched in the wpVPM as opposed to 365 in the ulVPM cells. Among the DEGs enriched in each population, we found genes previously identified as being involved in somatosensory development such as *Epha3*, *Sox2*, *Hs6st2*, *Cdh8*, or *Rora* enriched in wpVPM<sup>25–29</sup> or *Rorb*, *Slitrk6*, *Foxp2*, *Calb1*, or

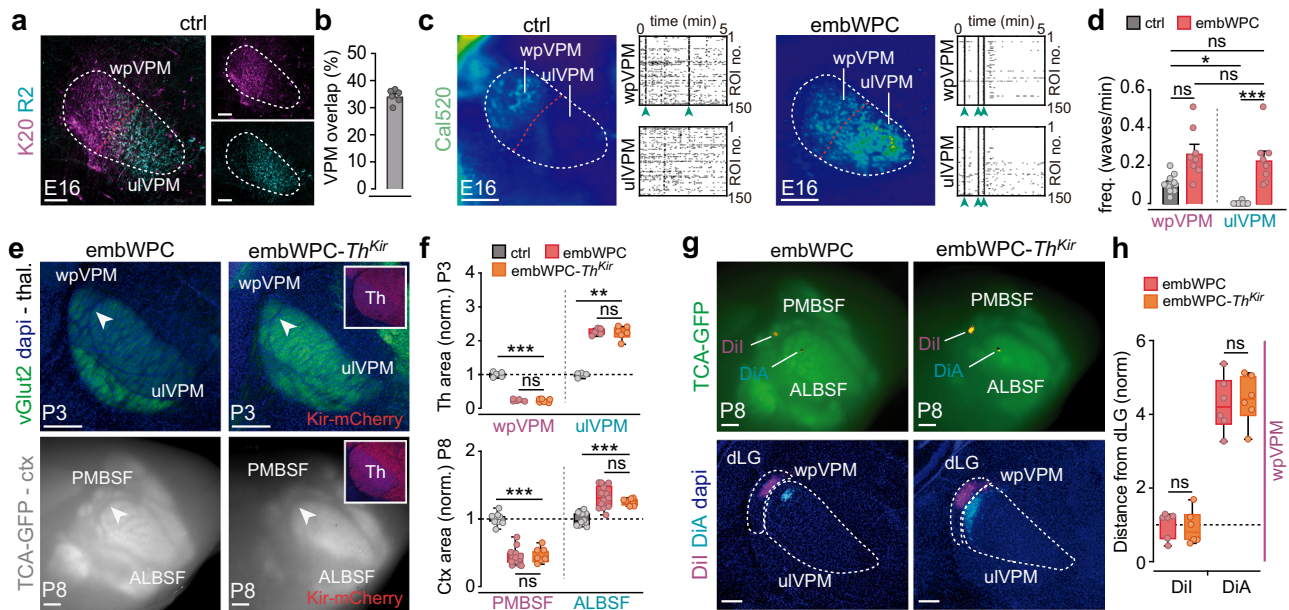


**Fig. 3 | ALBSF rescaling is independent of thalamic patterned activity.** **a** Coronal sections from the *Krox20-zsfgreen::R2-mCherry* double transgenic mouse showing Krox20-labeled axons (magenta, vPrV) and R2-labeled axons (cyan, dPrV) at the VPM at E16. **b** Quantification of the percentage of overlap of labeled axons ( $n = 6$ ). **c** Maximal projection of ex vivo spontaneous calcium activity in the prospective VPM sub-regions (wpVPM and ulVPM) in acute slices at E16. Raster plots of 5 min. The arrows label the calcium waves of synchronous activity. **d** Quantification of the frequency of wave activity in the VPM ( $n = 11$  ctrl,  $n = 8$  embWPC). **e** Upper panels, coronal sections of vGluT2 staining (green) in the wpVPM and ulVPM of embWPC and embWPC-*Th<sup>Kir</sup>* mouse (Kir-mCherry positive) at P3. Lower panels, surface view of TCA-GFP+ terminals in the PMBSF and ALBSF in embWPC and embWPC-*Th<sup>Kir</sup>* mice at P8. The arrows label the limits between wpVPM and ulVPM in the thalamus,

and PMBSF and ALBSF in the cortex. **f** Quantification of the data (Thalamus,  $n = 5$  ctrl,  $n = 5$  embWPC,  $n = 6$  embWPC-*Th<sup>Kir</sup>*; Cortex,  $n = 10$  ctrl,  $n = 13$  embWPC,  $n = 7$  embWPC-*Th<sup>Kir</sup>*). **g** Upper panels, Dil and DiA crystal placements in the PMBSF and ALBSF, respectively. Lower panels, backlabelled cells at the thalamus show shifted positions within the ulVPM thalamic area in both embWPC and embWPC-*Th<sup>Kir</sup>* mice at P8. **h** Quantification of the position of backlabelled cells with respect to the distance to the dLG nucleus. The gray horizontal dashed line in the graph represents the separation between wpVPM and ulVPM ( $n = 6$  embWPC,  $n = 6$  embWPC-*Th<sup>Kir</sup>*). Source data are provided as a Source data file. Scale bars, **a** 100  $\mu$ m; **c, g** (bottom) 200  $\mu$ m; **e** (top) 250  $\mu$ m, **e** (bottom), **g** (top) 500  $\mu$ m. Boxplots show the medians with the interquartile range (box) and range (whiskers). Bar graphs show the means  $\pm$  SEM. ns not significant. \* $p < 0.05$ , \*\* $p < 0.01$ , \*\*\* $p < 0.001$ .

*Lhx2*<sup>10,30–33</sup> enriched in the ulVPM (Supplementary Fig. 9b, c and Supplementary Data 1).

Then, we compared control versus embWPC transcriptional programs in the VPM. Remarkably, PCA analysis from ulVPM cells in an embWPC mouse indicated that these neurons grouped more closely with control wpVPM than control ulVPM (Fig. 4c and Supplementary Fig. 9d). This transcriptional shift was appreciated when the expression pattern of the upper lip and whisker-pad DEGs was plotted in the ulVPM of the embWPC (Fig. 4d). To investigate this effect, we trained a Support Vector Machine classifier (C-SVM) using differentially expressed genes and compared the results with the ulVPM-embWPC. This machine learning approach predicted that the cauterized model would be classified as the wpVPM control in 70% of cases, compared to 30% for the ulVPM control (Fig. 4e). Additionally, DEA against the wpVPM control revealed a much lower number of differentially expressed genes (93 DEGs) compared to the ulVPM control (268 DEGs) (Fig. 4f).

In total, 150 region-specific DEGs from ulVPM and wpVPM were significantly changed by the embWPC (Fig. 4g). Namely, in the ulVPM of the embWPC mouse, we observed an upregulation of ~17% of the DEGs normally expressed in the control wpVPM and downregulation of about 23% of control ulVPM DEGs, respectively (Fig. 4g, Supplementary Fig. 9e, and Supplementary Data 2). Notably, genes such as *Rora*, *Epha4*, *Hs6st2*, *Cdh9*, or *Pbxna2*, involved in axon guidance, thalamocortical mapping, and wpVPM development<sup>26,34</sup>, exhibited a wpVPM-like pattern in the ulVPM of embWPC mice (Fig. 4h, i and Supplementary Fig. 9f), also corroborated by in situ hybridization (Fig. 4j and Supplementary Fig. 9g). Next, we performed a Gene Ontology (GO) functional enrichment analysis of the genes with

expression changes in the ulVPM of the embWPC and identified 11 clusters of GO-Terms enriched in biological processes (BP) and molecular functions (MF) (Supplementary Fig. 10 and Supplementary Data 3). The top ranked cluster included 99 genes (46.8%) enriched in BP involved in dendrite development or synapse assembly (e.g., *Robo1* and *Flrt3*), and 12 genes (18.8%) enriched in MF involved in voltage-gated channel activity (e.g., *Kcnc2* and *Kcna1*).

Since the lack of spontaneous thalamic waves in embWPC-*Th<sup>Kir</sup>* mice did not prevent the ALBSF reorganization, we investigated whether the changes in ulVPM transcriptome are still observed in embWPC-*Th<sup>Kir</sup>* VPM. We conducted in situ hybridization for probes that we identified as wpVPM markers upregulated in the ulVPM of embWPC mice such as *Hs6st2*, *Rora*, and *Pou2f2*, or markers downregulated in the ulVPM of embWPC mice such as *Epha4*. Our results show a similar shift in the expression pattern for these genes in both embWPC and embWPC-*Th<sup>Kir</sup>* mouse (Supplementary Fig. 11) reinforcing that the transcriptomic changes in VPM territories are mainly independent of thalamic waves, activity. In summary, the spatial rescaling of cortical ALBSF territory in embWPC correlates with transcriptomic changes observed in upper lip thalamic input neurons, which shift towards a molecular signature resembling that of whisker pad input neurons (Fig. 4k).

### Increase of barrel size and functional spatial resolution of the cortical ALBSF map

We investigated whether upper lip-recipient thalamic neurons that acquire a whisker pad transcriptional profile during perinatal development might develop additional PMBSF characteristics later in life. At P8, PMBSF and ALBSF cortical areas differ in the average size of their

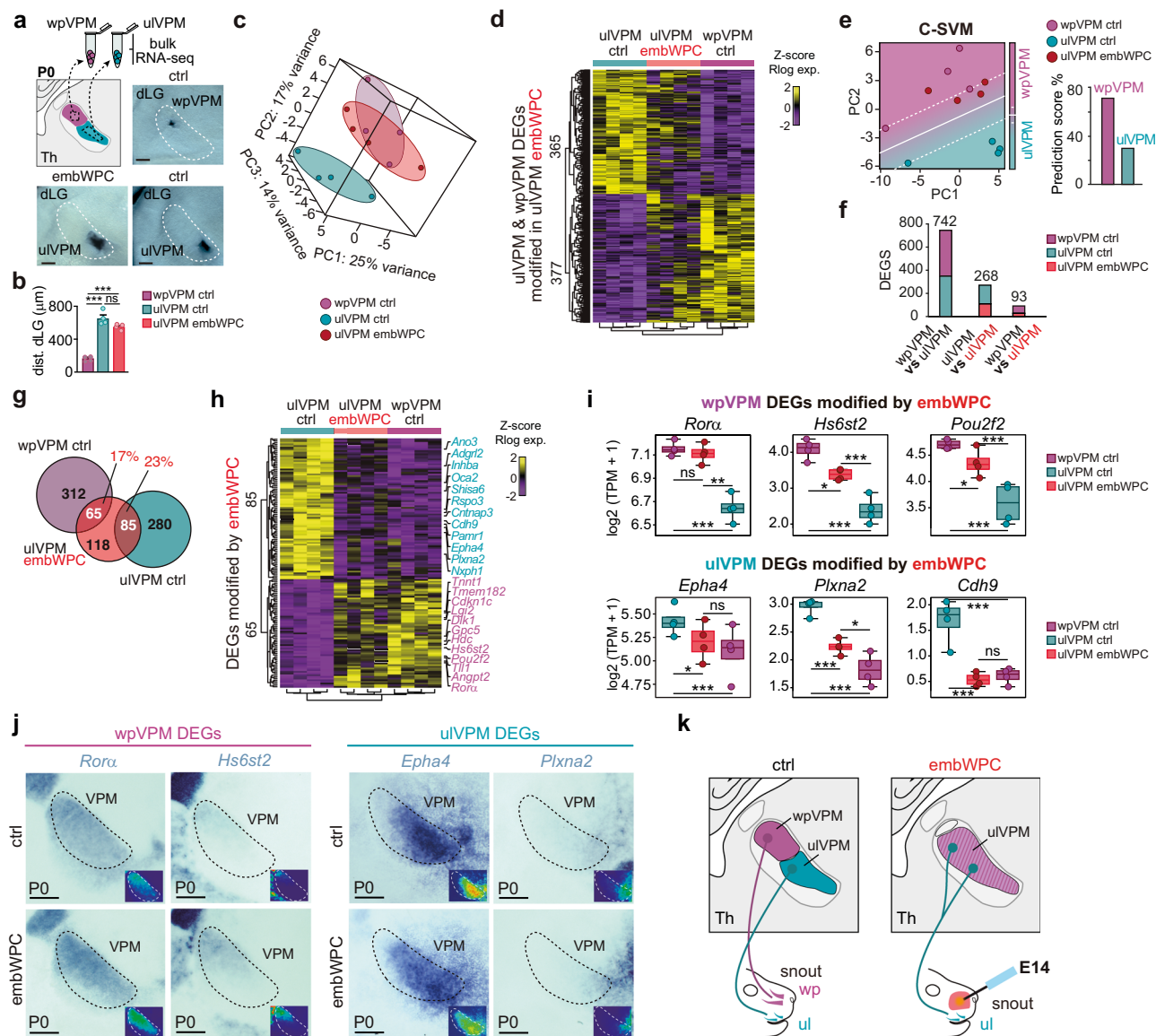


**Fig. 4 | Upper lip recipient thalamic neurons switch their transcriptional program to that of whisker-pad neurons.** **a** Top left, schema representing the paradigm. Top right and bottom, coronal images showing the dissected thalamic territories for sequencing. **b** Quantification of the dissected area with respect to the distance to the dLG nucleus ( $n = 4$  wpVPM-ctrl slices,  $n = 4$  ulVPM-ctrl slices, and  $n = 4$  ulVPM-embWPC slices, 4 mice per condition). **c** Principal component analysis (PCA) of wpVPM-ctrl ( $n = 4$ ), ulVPM-ctrl ( $n = 4$ ), and ulVPM-embWPC ( $n = 4$ ) at P0. **d** Heatmap of the normalized regularized logarithm (Rlog) Z-score of expression and unbiased clustering of region-specific DEGs showing their expression profile in the ulVPM of the embWPC at P0. The color code (yellow, high expression; purple, low expression) corresponds to the log2FC. **e** Left, C-support vector machine (C-SVM) analysis identifies the optimal demarcation plane between wpVPM (magenta dots) and ulVPM population (cyan dots). The ulVPM-embWPC samples are identified as wpVPM control based on its gene expression pattern (red dots). Right, the prediction score value of ulVPM-embWPC is classified as wpVPM

(70%) or ulVPM (30%) controls. **f** Number of differentially expressed genes (DEGs) obtained in their respective differential expression analysis. **g** Venn diagram shows the number of genes modified by embWPC in ulVPM overlapped in every subset of region-specific DEGs. **h** Heatmap of the normalized regularized logarithm (Rlog) Z-score of expression and unbiased clustering of region-specific DEGs whose expression was modified by embWPC in the ulVPM at P0. The color code (yellow, high expression; purple, low expression) corresponds to the log2FC. **i** Boxplots showing TPM expression levels of selected wpVPM-specific and ulVPM-specific DEGs modified by embWPC in the ulVPM. Boxplots show the medians with the interquartile range (box) and range (whiskers). **j** Coronal sections showing in situ hybridization of wpVPM and ulVPM DEGs at P0 ( $n = 5$  ctrl,  $n = 5$  embWPC, for each probe). **k** Schema illustrating the results. Source data are provided as a Source data file. VPM, ventroposterior medial nucleus. Scale bars, 200 μm. \*adj.  $p < 0.1$ , \*\*adj.  $p < 0.01$ , and \*\*\*adj.  $p < 0.001$ .

barrels and the extent of clustering of thalamocortical axons. Remarkably, we observed that, in addition to the overall increase in the cortical area occupied by the ALBSF, the average size of the cortical individual barrels in the ALBSF of the embWPC was significantly larger compared to the ALBSF control (Fig. 5a, b). This change appears to follow a gradient, with the largest ALBSF barrels located nearest to the remaining PMBSF (Fig. 5b). Furthermore, the cortical map of the expanded ALBSF gained definition and contrast as thalamocortical

terminals appeared more clustered within each barrel, and less innervating the barrel septa, resembling the control PMBSF (Fig. 5c–e). These differences in barrel size and contrast in the ALBSF map of the embWPC were not detected in POWPC mice (Fig. 5a–c).

Since thalamocortical input is a primary regulator of region-specific cortical features, we next investigated whether other cortical characteristics, besides barrel size and thalamocortical clustering, had also changed in the ALBSF cortex of the embWPC. The postnatal



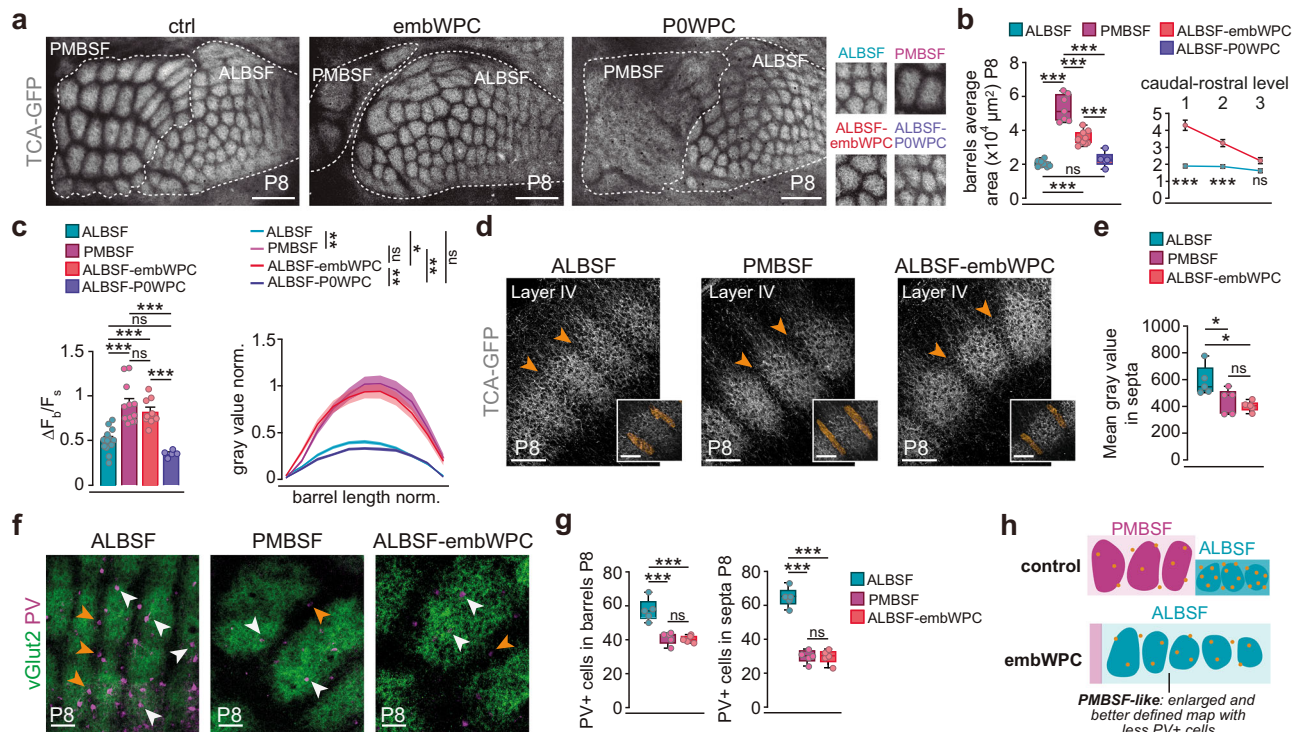


**Fig. 5 | ALBSF barrels acquire PMBSF cortical features.** **a** Cortical flattened tangential sections showing thalamocortical terminals (TCA-GFP+) in the PMBSF and ALBSF in control, embWPC and POWPC mice at P8. Insets show in detail the clustering of TCAs in each condition. **b** Left, quantification of the average area of 34 barrels ( $n = 7$  ctrl PMBSF,  $n = 9$  ctrl ALBSF,  $n = 9$  embWPC ALBSF,  $n = 5$  POWPC ALBSF). Right, quantification of the average area of 4 barrels per three caudal-to-rostral levels ( $n = 9$  ctrl ALBSF,  $n = 9$  embWPC ALBSF). **c** Left, quantification of the barrel/septum fluorescence ratio ( $\Delta F/F_s$ ) ( $n = 12$  ctrl PMBSF,  $n = 13$  ctrl ALBSF,  $n = 9$  embWPC ALBSF,  $n = 5$  POWPC ALBSF). Right, quantification of the gray value fluorescence intensity in a barrel ( $n = 66$  ctrl PMBSF barrels,  $n = 65$  ctrl ALBSF barrels,  $n = 42$  embWPC ALBSF barrels,  $n = 25$  POWPC ALBSF barrels). **d** Coronal sections showing thalamocortical terminals in layer IV in the ALBSF and PMBSF of

control, and ALBSF of embWPC mice. Insets showing the septa volume analyzed. **e** Quantification of the EGFP expression from TCA in septa of three barrels per animal (orange arrowheads in **d**) ( $n = 5$  ctrl ALBSF,  $n = 5$  ctrl PMBSF,  $n = 5$  embWPC ALBSF). **f** Cortical flattened tangential sections showing thalamocortical terminals (vGlut2+) and parvalbumin (PV) expression in barrel core (white arrowheads) and septa (orange arrowheads) in the ALBSF and PMBSF of control, and ALBSF of embWPC mice at P8. **g** Quantification of PV+ cells in four barrels and septa ( $n = 5$  ctrl ALBSF,  $n = 5$  ctrl PMBSF,  $n = 5$  embWPC ALBSF). **h** Schema illustrating the results. Source data are provided as a Source data file. Scale bars, **a** 500  $\mu\text{m}$ , **d** (insets) 80  $\mu\text{m}$ , **d** (insets) 80  $\mu\text{m}$ . Boxplots show the medians with the interquartile range (box) and range (whiskers). Bar graphs show the means  $\pm$  SEM. ns not significant. \* $p < 0.05$ , \*\* $p < 0.01$ , \*\*\* $p < 0.001$ .

PMBSF is known to contain fewer parvalbumin (PV) expressing interneurons in layer IV compared to the ALBSF<sup>35</sup>. Like in the PMBSF, we found significantly fewer PV-positive interneurons both in barrels and septa in layer IV of the ALBSF in the embWPC as compared to the ALBSF control (Fig. 5f, g). Hence, our findings demonstrate that, irrespective of receiving input from upper lip peripheral receptors, the VPM territory in embWPC adopts a molecular identity akin to that of a territory receiving input from mystacial whiskers. Consequently, it gains specific features of that circuit, including increased barrel size, better anatomical map definition, and fewer layer IV PV interneurons (Fig. 5h).

Next, we tested whether these anatomical reorganizations might have a functional correlate, for example, an enhanced topographical spatial resolution to upper lip stimulation. Thus, we carried out multi-point stimulations within the whisker pad or upper lip on both control and embWPC mice at P4 (Fig. 6a). On the control mice, cortical evoked responses confirmed a topographic organization of both PMBSF and ALBSF responses; however, while the PMBSF responses exhibited a well-defined and precise organization with virtually non-overlapping responses, those of the ALBSF were broader and less refined in comparison (Fig. 6b, c and Supplementary Movie 9). Thus, beyond their anatomical idiosyncrasies, cortical barrel subfields also have a distinct degree of functional map definition as they emerge during perinatal development. Interestingly, stimulations from distinct locations of the

upper lip of embWPC mice resulted in significantly less overlapping responses within the ALBSF (Fig. 6b, c and Supplementary Movie 10), suggesting enhanced spatial discrimination in the ALBSF of embWPC akin to that seen in the control PMBSF map.

Lastly, we investigated whether the rescaled ALBSF with enhanced resolution in the embWPC mice takes on PMBSF functions during somatosensory behavior in adulthood. To do this, we first conducted cFOS staining to label stimulated neurons in the ipsilateral and contralateral barrel subfields of embWPC mice after 10 min of exploring an enriched environment at P60 (Fig. 6d). Our immunostaining for cFOS revealed that, whereas in the ipsilateral (control) side the ALBSF was barely activated as compared to the PMBSF, the ALBSF was the predominantly activated region in the contralateral (cauterized) side after exploration (Fig. 6e, f). Therefore, we hypothesized that the rescaled ALBSF neurons of the embWPC mouse play a prominent role in vibrissae-driven sensory behavior in the adult. We conducted a texture discrimination test to evaluate tactile sensory processing, requiring adult mice to distinguish between novel and familiar textures (Fig. 6g, h). We used control mice, bilateral embWPC mice, and an additional control group where mystacial whiskers were bilaterally trimmed prior to testing. Our findings showed that embWPC mice discriminated textures as effectively as controls, while the trimmed group could not discriminate the new texture using only the remaining upper lip whiskers (Fig. 6i, j and Supplementary Fig. 12). These results

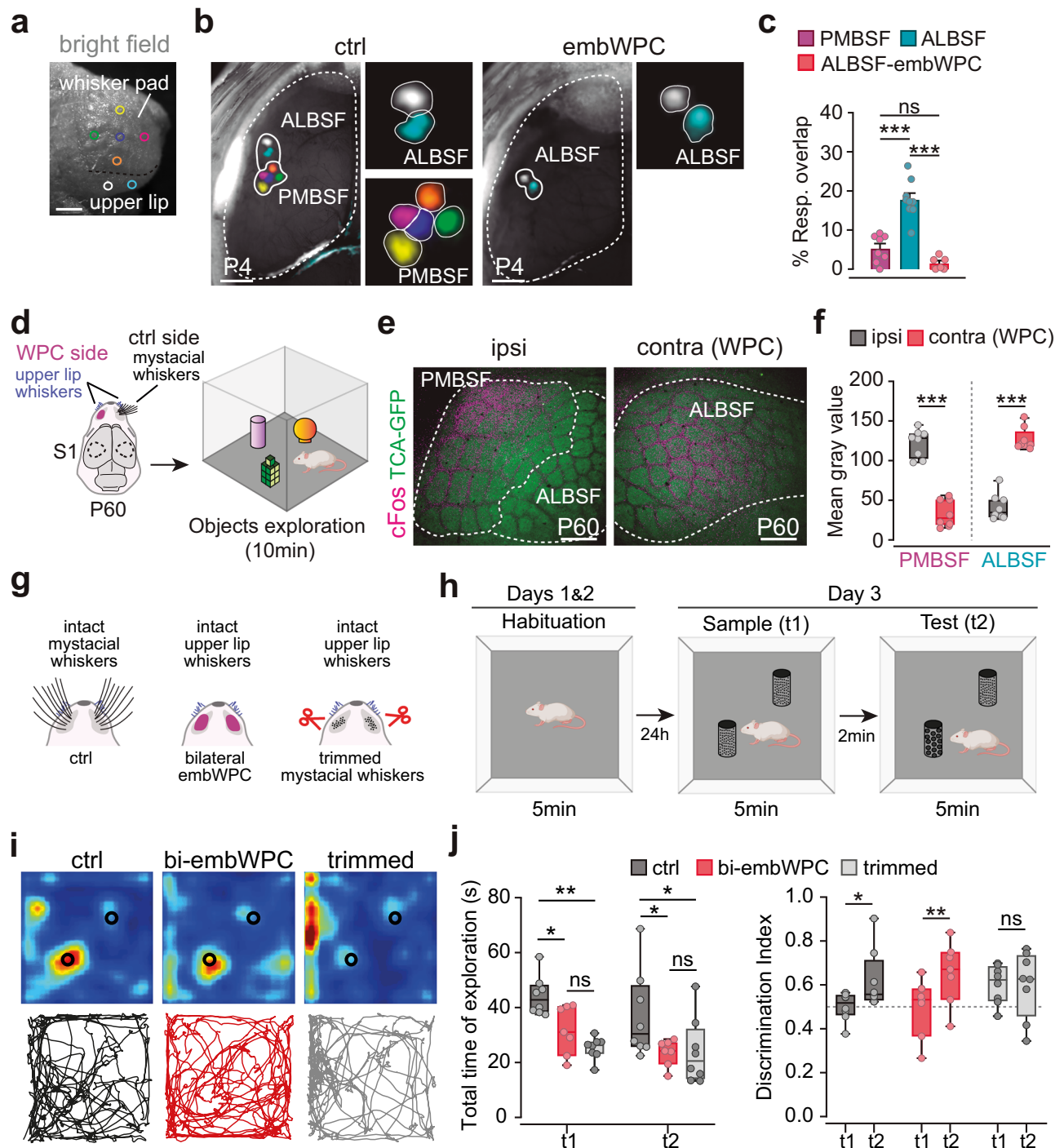


**Fig. 6 | Enhance ALBSF functional map in the postnatal embWPC mice.**

**a** Schema representing the experimental paradigm. **b** Cortical evoked responses (GCaMP6f) within the PMBSF and ALBSF to five distinct wps and two distinct uls in control and embWPC mice at P4. Dashed lines define the cortical hemisphere, and continuous lines indicate the territory covered by elicited responses.

**c** Quantification of the percentage of overlap between two distinct PMBSF and two distinct ALBSF responses at P4 ( $n = 8$  ctrl for PMBSF responses,  $n = 9$  ctrl for ALBSF responses,  $n = 6$  embWPC for ALBSF responses). **d** Schema representing the experimental paradigm.

**e** Cortical flattened tangential sections showing thalamocortical terminals and cFos expression in cortical ipsilateral (control) and contralateral (WPC) sides of P60 mice. **f** Quantification of the mean gray value of cFos expression ( $n = 8$  embWPC ipsi PMBSF,  $n = 8$  embWPC ipsi ALBSF,  $n = 8$  embWPC contra (WPC) PMBSF,  $n = 8$  embWPC contra (WPC) ALBSF).

**g** Schematic representation of the three experimental groups involved in the behavioral paradigm: mice with intact whiskers (ctrl  $n = 8$ ); mice with bilateral whisker pad cauterization

at E14 and intact upper lip whiskers (bi-embWPC  $n = 7$ ) and mice with trimmed mystacial whiskers and intact upper lip whiskers (trimmed  $n = 8$ ). **h** Schema representing the texture discrimination task protocol. **i** Representative heatmaps showing the distribution of snout positions during a 5-min test session for individual mice from each group (top), along with corresponding centroid trajectories (bottom). Warmer colors in the heatmaps denote regions with higher snout position frequency, highlighting areas of increased exploratory interest. **j** Left, boxplots comparing the total time that control, bi-embWPC and trimmed mice spent exploring textured objects across t1 and t2 sessions. Right, evaluation of texture discrimination performance comparing the discrimination index for each session. Source data are provided as a Source data file. Scale bars, **a** 1000  $\mu$ m and **e** 500  $\mu$ m. Bar graphs show the means  $\pm$  SEM. ns not significant. \* $p < 0.05$ , \*\* $p < 0.01$ , \*\*\* $p < 0.001$ . Mouse images were created in BioRender. Martini, F. (2025) <https://BioRender.com/l19k613>.



suggest that the rescaled ALBSF cortex in embWPC mice can support complex tactile discrimination, a function typically mediated by PMBSF neurons in adult mice under normal conditions.

## Discussion

Our study underscores the existence of a prenatal temporal window during mouse brain development that allows for the tuning of the size and definition of somatosensory cortical representations. Before cortical barrel fields are anatomically apparent, the thalamic VPM sub-territories exhibit specific transcriptional signatures at birth. Our results suggest that these signatures contribute to the distinct intra-modal anatomical and functional circuitry features specific to PMBSF and ALBSF cortical sub-territories.

Furthermore, our findings suggest that modulations in these transcription programs might enable intra-modal plasticity changes independently of the type of peripheral receptors. In mice lacking the mystacial whiskers, VPM neurons receiving upper lip whisker input can shift their transcriptional features toward a whisker pad-like program, reconfiguring thalamocortical circuits and cortical features to resemble a PMBSF. These changes increase barrel size and functional spatial resolution, thereby enhancing spatial discrimination in regions such as the ALBSF, where cortical representations were otherwise less defined.

The developmental relationship between sensory receptors and somatosensory representations has been thoroughly examined in prior work involving mice and rats. Embryonic ablation of the forelimb in rats resulted in the expansion of S1 representation of the hindlimb without altering the sensory receptors of the spared peripheral region<sup>36</sup>. Moreover, deprivation of a single whisker or a row of whiskers during the first postnatal week, leads to the loss of the corresponding cortical barrels and enlargement of the surrounding barrels<sup>37–42</sup>. And remarkably, rewiring of ipsilateral trigeminal input from mystacial whiskers to the ipsilateral barrel field generates an ectopic barrel field within the normal barrel map<sup>43</sup>. Collectively, these studies highlight the sensitivity of somatosensory regions and barrel maps to manipulations in peripheral or sensory input but also question a direct correlation between the size of cortical barrels and their corresponding peripheral sensory receptors. Our results in the embWPC model define a developmental window for an intra-modal barrel field reorganization, showing that only embryonic, and not postnatal, ablation of the whisker pad induces the ALBSF anatomical and functional enlargement. This reorganization capability is, therefore, temporally constrained during prenatal development and anticipates the closure of the critical time window for somatosensory circuits<sup>39,44</sup>.

Thalamic spontaneous activity is key for the emergence of cortical somatosensory maps, as evidenced by the fact that suppressing this activity leads to mice that do not develop barrels despite having normal whiskers<sup>21</sup>. Moreover, in early blind pups, cross-modal changes in activity-dependent gene regulation in VPM neurons correlate to changes in barrel size<sup>10</sup>. Here, we observed a striking intra-modal prenatal reorganization of the frequency and pattern of thalamic waves between VPM subfields in embWPC mice. The ulVPM significantly increased the frequency of thalamic waves compared to control mice. This change in activity pattern might serve as a mechanism to enhance ulVPM barrel size and definition and, in turn, to map these activity-dependent features onto the cortical ALBSF during development. This hypothesis could not be directly tested, as thalamocortical axons in the embWPC-*Th<sup>Kir</sup>* mice, in which spontaneous thalamic waves are blocked, fail to cluster in layer IV in both PMBSF and ALBSF, as previously described in *Th<sup>Kir</sup>* mice<sup>21</sup>.

Notably, using embWPC, we could show that the enlargement of the cortical ALBSF area is guided by the thalamus in an activity-independent manner. Indeed, in embWPC-*Th<sup>Kir</sup>* mice, lacking synchronous thalamic activity, the rescaling of the ALBSF still occurs. Moreover, we show that the PrV input reorganizes in the embWPC

VPM. Therefore, we propose that remapping within the PrV, initiated at E14 following whisker pad ablation, may significantly influence the development and organization of thalamocortical axons, subsequently affecting thalamic and cortical map reorganization.

Remarkably, our study revealed that thalamic neurons can shift their transcriptional profile intra-modally. We found that the transcriptional profile of ulVPM neurons in embWPC mice mirrors that of the wpVPM neurons in control mice. Crucial genes for thalamocortical barrel field development, such as *Rora* or *Epha4*<sup>26,34</sup>, accordingly altered their expression pattern in the ulVPM neurons innervating the ALBSF. For instance, we observed an upregulation of *Rora* in this region, suggesting a potential role in increasing the density and clustering of axonal terminals in layer IV in the ALBSF of the embWPC mice. An activity-dependent upregulation of *Rorb*, a related orphan receptor, in VPM neurons, has been shown to mediate an increased clustering of thalamic axons in S1<sup>10</sup>. ulVPM neurons adopting a region-specific wpVPM transcriptional profile might serve as an intrinsic mechanism to switch a PMBSF developmental program, ensuring an enhanced anatomical and functional definition of thalamocortical axons in the ALBSF cortical barrel map. Additionally, we identified alterations in genes directly associated with neuronal activity<sup>45,46</sup>, including ion channels, which may contribute to or reflect the modified pattern of thalamic activity observed in the embWPC model. Yet, it remains to be determined whether the acquisition of wpVPM-like molecular identity by ulVPM neurons is dependent on thalamic spontaneous activity.

Large barrels in the PMBSF correspond to long mystacial whiskers<sup>12,13</sup>, whereas ALBSF barrels relate to the short whiskers on the upper lip of the snout and are comparatively smaller, less defined, and densely packed<sup>9,47,48</sup>. Moreover, although the average volume of a single barrel in the ALBSF is smaller than in the PMBSF, the numerical density of parvalbumin (PV)-positive interneurons is higher in ALBSF than in the PMBSF<sup>35</sup>. Somata of PV neurons in the barrels and septa of the ALBSF are reported to receive more vesicular glutamate transporter Type 2-labeled (vGlut2) boutons than those in the PMBSF, suggesting the presence of more potent feedforward inhibitory circuits in the ALBSF<sup>35</sup>. Behaviorally, mystacial vibrissae hold significant behavioral relevance for the animal, being the first ones used for search of objects and gaps, and to discern diverse tactile features such as object position, shape, or texture<sup>49</sup>. Although the function of upper lip shorter whiskers remains largely unexplored, they appear to primarily aid in object discrimination when the snout is near the object<sup>8,50–52</sup>. Given these anatomical and functional disparities, the PMBSF and ALBSF represent two distinct somatosensory subsystems. Consequently, we initially expected minimal reorganization of the ALBSF upon deprivation of the whiskers corresponding to the PMBSF. However, our data from the embWPC mice revealed a notable anatomical reorganization within the ALBSF, leading to the formation of large and well-defined barrels and a decreased density of PV interneurons at the postnatal life. Additionally, our in vivo functional data revealed that this reorganization might contribute to enhance functional resolution of the ALBSF map to point-to-point peripheral stimulations. Our texture discrimination experiments demonstrated that embWPC adult mice, in which the small upper lip whiskers remain intact, can adopt specialized mystacial whisker functions and discriminate between distinct textures as effectively as control mice.

Altogether, these findings highlight a decoupling of mechanisms governing the type, size, and density of sensory peripheral receptors from those influencing the size and definition of cortical representations that might involve adopting subcortical- and subregion-specific transcriptional programs. Specifically, we observed that the prenatal thalamus possesses plasticity mechanisms to drive the development of a barrel field with anatomical and functional features akin to the PMBSF, regardless of the type of peripheral receptor. Therefore, our findings indicate that the brain may still construct a barrel map capable

of processing intricate tactile functions for the animal, even in scenarios involving the availability of only small receptors with subsidiary functions.

## Methods

### Mouse strains

All animal experiments were conducted in accordance with the Committee on Animal Research at the University Miguel Hernández that approved all the animal procedures, which were carried out in compliance with Spanish and European Union regulations. Similar numbers of male and female mice were used interchangeably. No sex-related differences were observed in the measurements throughout the study. Mice were maintained in pathogen-free facilities under standard housing conditions with continuous access to food and water on a 12 h light-dark cycle. The number of animals used in each experiment is noted in the figure legends.

All mouse transgenic lines in this study were maintained on an ICR/CD-1 genetic background and genotyped by PCR. The *TCA-GFP Tg*, in which the TCAs are labeled with GFP, the *R26<sup>Kir2.1-mCherry</sup>* mouse lines were previously described<sup>10,14,21</sup>. The Cre-dependent mouse line, *R26<sup>GCaMP6f</sup>* was obtained from Jackson Laboratories (Stock number 024105) and crossed with an *Emx1<sup>Cre/+</sup>* transgenic mouse<sup>53</sup> to conditionally express the fast calcium indicator GCaMP6f in glutamatergic cortical neurons (*Emx1<sup>GCaMP6f</sup>*)<sup>21,22</sup>. The *R26<sup>Kir2.1-mCherry</sup>* mice were crossed with an inducible *Cre<sup>ERT2</sup>* mouse line driven by *Gbx2*, an early specific thalamic promoter (*Gbx2<sup>CreERT2/+</sup>*)<sup>54</sup>. Double mutants are referred to as *Th<sup>Kir</sup>* and triple mutants as *TCA-GFP-Th<sup>Kir</sup>*<sup>21</sup>. Tamoxifen induction of Cre recombinase in the double/triple mutant embryos was performed by gavage administration of tamoxifen (5 mg dissolved in corn oil, Sigma) at E10 to specifically target all primary sensory thalamic nuclei. Tamoxifen administration in pregnant mice produces non-desirable side effects such as delivery problems and decrease survival of newborn pups<sup>55</sup>. To increase the survival rate of young pups, we administered 125 mg/Kg of progesterone (DEPO-PROGEVERA®) intraperitoneally at E14 and implemented a C-section procedure at E19. Pups were then placed with a foster mother. In all cases, the *Cre<sup>ERT2</sup>*-negative littermates were used as controls of the experimental condition. The *r2<sup>mCherry</sup>*<sup>19</sup>, *Krox20<sup>Cre</sup>*<sup>56</sup>, and *R26RZsGreen* (Jackson Laboratories, Stock number 007906)<sup>57</sup> lines, were as described. We crossed *Krox20<sup>Cre</sup>* with *R26RZsGreen* to generate double transgenic *Krox20<sup>ZsGreen</sup>* mice, and we also generated *Krox20<sup>ZsGreen</sup>;;r2<sup>mCherry</sup>* triple transgenic mice.

### Histology

For in situ hybridization and immunohistochemistry at postnatal stages, mice were perfused with 4% paraformaldehyde (PFA) in PBS (0.01 M), and their brains were subsequently removed and post-fixed in the same fixative overnight. For the immunohistochemistry of embryonic tissue, the brains were dissected and immediately fixed in 4% PFA overnight. For Nissl staining, a microtome (MICROM) was used to cut paraffin slices of 5 µm. Next, the sections were stained in 0.5% cresyl violet (Sigma) solution for 15–25 min and then rinsed quickly in distilled water. After decolorization in 70% ethyl alcohol for few seconds, the sections were dehydrated in 95%, 100% ethyl alcohol for 2 to 3 min, cleared in xylene (Sigma) for 2 min and mounted with Eukitt (Merk). Cytochrome oxidase staining was performed to label the PrV territories. For cytochrome Oxidase (CytOx) staining, 80 µm vibratome coronal sections were incubated overnight at 37 °C in a CytOx solution: 0.03% cytochrome c (Sigma C2506), 0.05% 3-3' diaminobenzidine tetrahydrochloride hydrate (DAB, Sigma D5637) and 4% sucrose in PBS. For tangential sections, cortical hemispheres were flattened and cryoprotected through steps of 10, 20, and 30% of sucrose in PBS. Then, a cryotome (MICROM) was used to cut at 80 µm tangential sections. Immunohistochemistry was performed on 80 µm vibratome or cryotome brain sections (coronal and tangential), which were first incubated for 1 h at room temperature in a blocking solution

containing 1% BSA (Sigma) and 0.25% Triton X-100 (Sigma) in PBS. Afterwards, the slices were incubated overnight at 4 °C with the following primary antibodies: guinea pig anti-vGluT2 (1:10000, Synaptic Systems, 135404), chicken anti-GFP (1:3000; Aves Labs, GFP-1020), rat anti-RFP (1:1000, Chromotek, 5F8), rabbit anti-cFos (1:500, Synaptic Systems, 226003), rabbit anti-PV (1:5000, Swant PV27), and rabbit anti-RFP (1:1000, Rockland, 600-401-379). Sections were then rinsed in PBS and incubated for 2 h at room temperature with secondary antibodies: Alexa488 donkey anti-guinea pig (1:500, Thermo Fisher, A11073), Alexa488 goat anti-chicken (1:500, Thermo Fisher, A11039), Alexa594 donkey anti-rat (1:500, Thermo Fisher, A21209) and Alexa goat 568 anti-rabbit (1:500, Invitrogen, A11011). Counterstaining was performed using the fluorescent nuclear dye 4',6-diamidino-2-phenylindole (DAPI) (Sigma). In situ hybridization was performed on 60 µm vibratome sections using digoxigenin-labeled antisense probe for *Rora*, *Epha4*, *Pou2f2*, *Hs6st2*, *Plxna2*, and *Cdh9*. Hybridization was carried out overnight at 65 °C, and after hybridization, the sections were washed and incubated overnight at 4 °C with an alkaline phosphatase-conjugated anti-digoxigenin antibody (1:2500–1:4000, Roche). To visualize the RNA-probe binding, a colorimetric reaction was performed for 1–2 days at room temperature in a solution containing NBT (nitro-blue tetrazolium chloride, Roche) and BCIP (5-bromo-4-chloro-3-indolyl phosphate p-toluidine salt, Roche). After development, the sections were washed and mounted in Glycerol Jelly (Merck Millipore). Images were acquired with a Leica DFC550 camera in a Leica DM5000B microscope, a Leica K5 camera in a Leica DMI8 microscope, or with an AxioScan Z1 widefield microscope (Zeiss).

### Immunolabeling-enabled three-dimensional imaging of solvent-cleared organ (iDISCO+)

The whole mount for the iDISCO+ protocol was conducted following the previously described methods<sup>58,59</sup>. After perfusing mice with 4% PFA, heads (without any dissection) were dehydrated using a series of methanol concentrations (50, 80, 100, and 100%) and subsequently incubated overnight in 6% H<sub>2</sub>O<sub>2</sub> in methanol to bleach the samples. Following this, heads were incubated in Permeabilization solution (Triton X-100, Glycine, DMSO) and blocked with Blocking solution (Triton X-100, Donkey Serum, DMSO) for 2 days, respectively. For the clearing process, heads underwent dehydration in methanol (20, 40, 60, and 80%) at room temperature on a rotating shaker. Specimens were then immersed twice in 100% methanol for 1 h and treated overnight in 1/3 volumes of 100% dichloromethane (DCM; Sigma-Aldrich; 270997). On the subsequent day, heads were incubated in 100% DCM for 30 min. Finally, samples were cleared in 100% dibenzyl ether (DBE; Sigma-Aldrich; 108014) until they became translucent.

### Ultramicroscopy and image processing

3D imaging was primarily performed with an ultramicroscope I (LaVision BioTec) using InspectorPro software (LaVision BioTec). The light sheet was generated by a laser (wavelength 488 nm, LaVision BioTec). A binocular stereo microscope (MXV10, Olympus) with a 23x objective (MVPLAPO, Olympus) was used at different magnifications (1.25x). Samples were placed in an imaging reservoir made of 100% quartz (LaVision BioTec) filled with ethyl cinnamate and illuminated from the side by the laser light.

Images were generated using Imaris x64 software (version 9.3.1, Bitplane). Stack images were first converted to Imaris files (.ims) using ImarisFileConverter. The whisker pad and upper lip area reconstruction were generated by creating a mask around each one using the “surface tool” and they were pseudo-colored (whisker pad area in magenta and upper lip area in cyan). Each individual follicle was isolated also manually using the same tool, selecting nine follicles arbitrarily at three different points from medial to lateral. The septa volume reconstruction from coronal sections of 80 µm was generated

by creating masks around each barrel using the “surface tool” and they were pseudo-colored (orange).

### In utero and postnatal whisker pad cauterization

Embryonic unilateral and bilateral whisker pad cauterization (embWPC and bi-embWPC, respectively) were performed at E14 as described previously for enucleation<sup>10</sup>. Dams were deeply anesthetized with isoflurane, and the uterine horns were exposed through a midline laparotomy. Using a fiber optic light source, embryos were visualized within the uterus. The whisker pads of selected embryos were then cauterized with a 0.1 mm platinum wire (Thermo Fisher) connected to a cautery unit. All follicles within the whisker pad were carefully cauterized. After cauterizing half of the litter, the embryos were returned to the abdominal cavity, the surgical incision was closed, and the embryos were allowed to develop until either E18 or postnatal stages. Postnatal unilateral whisker pad cauterization (POWPC) was performed on P0 pups. Animals were deeply anesthetized on ice. The right whisker pad was cauterized under the loupe to specifically burn the principal whisker follicles. Pups were then warmed up to 37 °C on a heating pad, before being returned to the mother.

### Measurement of brain areas and data analysis

ImageJ software was used to measure the size of individual barrels, barrel field territories in the cortex, thalamus and brainstem, as well as the snout areas in slices. For barrel field territories and snout areas data were normalized. Each barrel field or snout area from a given experimental condition was normalized to the corresponding barrel field or snout mean area in the control, which was considered as 1. For the snout measurements, the skin of the snout was flattened and post-fixed in 4% PFA. Paraffin slices of 5 µm were obtained to quantify the number of follicles and the upper lip snout area using Nissl staining. We measured two slices per animal, one medial and one more lateral, and calculated the average. To quantify the number of cells in the vPrV, dPrV, PrV, wpVPM, ulVPM, and VPM regions, we counted DAPI-stained nuclei within a 55.35 µm<sup>2</sup> region of interest (ROI) in 80 µm coronal sections. This cell count was extrapolated to estimate the total number of cells in each target area. Four slices per animal were analyzed, and the cell count across these slices were summed. TCA-GFP mouse was used for the quantifications of the barrel field definition in flattened tangential sections, barrel field areas in toto and thalamic territories in slices. To assess the rostro-caudal gradient of increased barrel size in embWPC mice, we analyzed three distinct levels along the caudal-to-rostral axis, measuring four barrels per level and calculating the average. The most caudal level was positioned near the remaining PMBSF territory, the most rostral near the SI rostral boundary, and the medial level at the midpoint between these two. For thalamic rescaling analysis, we examined brain slices at P3, when barreloids become more prominent, facilitating anatomical analysis. For cortical barrels analysis, we chose P8, as barrels are well-established at this stage, allowing for clearer visualization and analysis. To quantify the size of cortical areas in toto, TCA-GFP (control, embWPC, POWPC, and embWPC-*Th<sup>Kir</sup>*) mice were perfused and directly processed to obtain images under the stereo fluorescent microscope (Leica MZ10 F). Coronal serial slices of 80 µm were obtained from TCA-GFP brains, and thalamic barrel field territories were immunolabeled with GFP and vGlut2 in order to better detect the areas. For  $\Delta F_b/F_s$  quantifications, we used ImageJ to measure the gray value of EGFP labeling in barrels of flattened tangential sections.  $\Delta F_b/F_s$  was calculated using the maximum value of the baseline signal average as  $F_s$  in single barrels. To measure the gray value, we used a 20-width segmented line, covering five barrels per condition, and calculated the average. To compare the barrel profile for the different conditions, we normalized each barrel's gray values to the lowest number (septa), which was considered 0. Next, we took 11 gray value data points per barrel to normalize the length for all the conditions. To quantify the mean gray value in septa, coronal serial slices of

80 µm were obtained from TCA-GFP brains, and barrels from PMBSF and ALBSF (control and embWPC) were immunolabeled with GFP to measure the fluorescence of three barrels of septa per condition using Imaris x64 software, and calculated the average. For PV+ cells quantifications in PMBSF and ALBSF barrels and septa, we counted the number of PV+ cells within four barrels, and their septa for each condition in flattened tangential sections of 80 µm immunolabel with PV and vGlut2. We quantified cFos expression within PMBSF and ALBSF layer IV in flattened tangential sections of 80 µm immunolabel with cFos. The region of interest (ROI) was a square of 600 × 1000 µm on each territory measuring the mean gray value.

### Dye-tracing studies

For axonal tracing, animals were perfused with 4% PFA in PBS. Heads were post-fixed overnight to trace innervation from the snout to the trigeminal nucleus, while brains were dissected and post-fixed overnight to trace thalamocortical axons. Small DiI (1,1'-diiododecyl-3,3,3',3'-tetramethylindocarbocyanine perchlorate; Invitrogen), DiA (4-[4-(dihexadecylamino) styryl]-N-methylpyridinium iodide; Invitrogen) and DiD (1,1'-diiododecyl-3,3,3',3'-tetramethylindocarbocyanine, 4-chlorobenzenesulfonate salt; Invitrogen) crystals were inserted under a stereo fluorescence microscope (MZ10 F, Leica) into the PMBSF, ALBSF, vPrV, dPrV, the whisker pad and upper lip. The dye was allowed to diffuse at 37 °C in PFA solution for 4 to 8 weeks to trace the innervation from the snout to the PrV, and 6 weeks to trace from the vPrV and dPrV to the VPM. To trace the thalamocortical pathway, small DiI and DiA crystals were inserted into distinct PMBSF barrels (C2, C3, D3, and C4) and DiI, DiA, and DiD crystals were placed into ALBSF territory. To reveal the PMBSF and ALBSF, a TCA-GFP transgenic specific mouse line was used. The dye was allowed to diffuse at 37 °C in a PFA solution for 3 weeks. Vibratome sections (80 µm thick) were obtained and counterstained with the fluorescent nuclear dye DAPI (Sigma-Aldrich). Three sections per animal were imaged using a Leica K5 camera in a Leica DMi8 microscope. Image analysis was performed on ImageJ. To quantify the translocation of the backlabeling in the VPM, the distance from the dorsolateral geniculate (dLG) nucleus border was measured to the center of the backlabeled cells in the VPM. The distance from the dLG nucleus border to the separation between wpVPM and ulVPM was determined following the barreloid rows in the VPM of ctrl mice.

### Measurement of PrV axons overlap in VPM and data analysis

To label rhombomere 3-derived vPrV neurons, we used the *Krox20<sup>Cre</sup>* line<sup>56</sup> to drive the Rosa-ZsGreen reporter (*R26RZsGreen*)<sup>60</sup>, whereas to label rhombomere 2-derived dPrV neurons, we used the *r2<sup>mCherry</sup>* reporter line<sup>19</sup>. Brains from *Krox20<sup>Cre</sup>; R26RZsGreen*; *r2<sup>mCherry</sup>* animals, in which vPrV and dPrV projections are labeled simultaneously, were collected at embryonic stages (E16.5, E18.5) and postnatal stages (P0, P4, and P8) for analysis. Embryonic brains were directly post-fixed in 4% PFA in PBS, while postnatal brains were perfused before post-fixation in the same fixative. Brains were cut on a Vibratome (Leica) at 60 µm thickness throughout the VPM and PrV. To enhance the *r2::mCherry* signal, the sections were stained with a rabbit anti-RFP primary antibody (1:1000, Rockland, 600-401-379) coupled with an anti-rabbit Alexa 568 secondary antibody (1:500, Invitrogen, A11011), while the endogenous ZsGreen fluorescence was not amplified. At least five sections per animal were imaged using Axioscan Z1 widefield microscope (Zeiss), using a 10x (NA = 0.45) plan-APOCHROMAT objective. Subsequent image analysis was conducted using ImageJ. To quantify the percentage of overlap of vPrV-dPrV axons in the VPM, a wand tool connecting pixels of the same intensity level in a 15-pixel range, was used to automatically delineate the innervation area of *Krox20+* and *R2+* axons, generating the Regions of Interest (ROIs). Subsequently, the overlapping area and the total innervation area of both *Krox20+* and *R2+* axons were measured with the measure tool in ImageJ to calculate the percentage of overlap of PrV axons in the VPM.



### In vivo mesoscale calcium imaging

As previously described<sup>22</sup>, embryos at E18 were extracted from the uterus and maintained at 35 °C. E18 pups were immobilized using soft clay. P4 mice underwent anesthesia with ice, followed by surgical removal of the scalp. A 3D-printed plastic holder was attached to the skull using cyanoacrylate adhesive and dental cement, then affixed to a ball-joint holder to stabilize the head. To maintain body temperature, pups were placed on a controlled temperature heating pad, ensuring a range of 32–34 °C. For recording calcium activity, we used a 16-bit CMOS camera (ORCA-Flash 4.0, Hamamatsu) coupled to a stereo microscope (Stereo Discovery V8, Zeiss), which offered 470 nm LED illumination. For *Emx1*<sup>CaMPeF</sup>, images were acquired with a frame size of 1024 × 1024 pixels using a macro magnification of 1.6x at E18 and of 1.25x at P4, resulting in a spatial resolution of 8.12 μm/pixel and 10.64 μm/pixel, respectively. Image frames were captured continuously at a rate of 3.33 frames per second (300 ms frame period) for *Emx1*<sup>CaMPeF</sup>, with an average of three movies acquired per animal.

### In vivo mechanical stimulation of the whisker pad

We conducted somatosensory stimulations by touching the whisker pad and upper lip using a 0.16 g von Frey filament (TouchTest®, BIO-SEB). Each animal was stimulated at least three times, with intervals of 5 min between each stimulus. Subsequently, we calculated the size of responses in the PMBSF and ALBSF elicited by whisker pad and upper lip stimulations.

### Analysis of the evoked activity in vivo

For the assignment of cortical territories, the perimeters of the PMBSF and ALBSF were determined using the cortical responses elicited by mechanical stimulation of five sites on the whisker pad, as previously described<sup>21,22</sup>, and two or three sites of the upper lip. At embryonic day (E)18, the perimeters were predicted by scaling down and superimposing the limits of the sensory territories observed in the TCA-GFP transgenic line<sup>44</sup> at P2, as previously detailed<sup>22</sup>, and using the responses to whisker pad and upper lip stimulations as reference for PMBSF and ALBSF, respectively. Image analysis was performed with ImageJ. The mean fluorescence of five frames just prior to the stimulation established FO (baseline fluorescence), and a ΔF/FO time series was then generated from the raw data and subsequently transformed into 8-bit images before processing with a 2-pixel diameter Gaussian filter. A maximum intensity projection of all frames containing evoked responses was obtained. The boundaries of the response were defined using the wand tool, connecting pixels of the same intensity level within a 15-pixel range, and the area of each response was calculated using the measure tool in ImageJ. To measure the active fraction of PMBSF and ALBSF in embWPC mice at E18 and P4, the control side was used to delineate the PMBSF and ALBSF territories following stimulation of the whisker pad or upper lip, respectively. On the WPC side, these areas were superimposed using the mirror image from the control side. The PMBSF and ALBSF active fractions were determined by measuring all elicited responses within each territory and calculating the percentage of the PMBSF and ALBSF theoretical areas occupied by these responses following whisker pad or upper lip stimulations. To quantify the percentage of overlap between responses following the whisker pad and upper lip stimulations (%PMBSF-ALBSF overlap) at E18 and P4, the overlap between all elicited responses following the whisker pad and those following upper lip stimulations was calculated. To quantify the percentage of overlap within PMBSF or ALBSF (% Responses overlap) in ctrl and embWPC, the overlap for two different stimuli on the whisker pad or two different stimuli on the upper lip was calculated.

To visualize the evoked stimuli in different color profiles for the generation of supplementary movies, we utilized custom scripts developed in Matlab<sup>TM</sup>. These scripts were adapted from the image

analysis suite WholeBrainDX (referenced in the Data and code availability section). For each movie, frames containing movement artifacts, spontaneous activity, and calcium activity deemed as stimulation byproducts were excluded. Baseline correction was performed using the built-in Matlab function “msbackadj” with a window size of 20 and a step size of 20. Subsequently, ΔF/FO was computed using the median value of the corrected signal as FO. Movie segmentation and calcium event detection followed the method described<sup>61</sup>. Image segmentation and generation of a binary movie involved Gaussian smoothing with an 80 μm distance and a signal intensity threshold. The binary movie was color-labeled using ImageJ software and customized with a Gaussian filter. Subsequently, the original movie and the color-coded binary movie were merged using the “Image Calculator” function in ImageJ.

### Microdissection and RNA isolation for RNA-seq

To capture gene expression changes during the critical period of somatosensory map plasticity, we collected tissue from the wpVPM and ulVPM territories of P0 ctrl and embWPC pups. Pups were euthanized by decapitation, and their brains were dissected under RNase-free conditions to prevent RNA degradation. The brains (five brains were pooled for each sample) were collected in ice-cold KREBS solution and sliced into 300 μm sections using a vibratome (VT1000S Leica). The wpVPM and ulVPM territories were rapidly microdissected under a stereo microscope. The bulk tissue was immediately transferred to the lysis buffer of the RNeasy<sup>®</sup> Micro Kit (Qiagen, 74004) for total RNA extraction, following the manufacturer’s instructions. RNA quality was measured for all samples using an Agilent Bioanalyzer 2100 system, and only samples with RNA integrity number (RIN) >8 were used for library construction.

### Library preparation and RNA sequencing

Library construction and sequencing were performed at Novogene Co. Ltd. Genomics core facility (Cambridge, UK). cDNA multiplex libraries were prepared using a custom Novogene NGS RNA Library Prep Set (PT042) kit. Briefly, mRNA was purified from total RNA using poly-T oligo-attached magnetic beads. After fragmentation, the first strand cDNA was synthesized using random hexamer primers followed by the second strand cDNA synthesis. The library was ready after end repair, A-tailing, adapter ligation, size selection, amplification, and purification.

The library was checked with Qubit and real-time PCR for quantification and bioanalyzer for size distribution detection. Libraries were pooled and sequenced in 2x150bp paired-end mode on an S4 flowcell in the Illumina Novaseq6000 platform. A minimum of 40 million reads were generated from each library.

### Bioinformatic analysis of the RNA-seq

RNA-seq analysis were performed as previously described<sup>62</sup> with minor modifications: quality control of the raw data was performed with FastQC (v.0.11.9). RNA-seq reads were mapped to the Mouse genome (GRCm39) using STAR (v2.7.9a)<sup>63</sup> and SAM/BAM files were further processed using SAMtools (v1.15). Aligned reads were counted and assigned to genes using Ensembl release 104 gene annotation and FeatureCounts, Subread (v2.0.1). Normalization of read counts and differential expression analyses were performed using DESeq2 (v1.32)<sup>64</sup>, Bioconductor (v3.15)<sup>65</sup> in the R statistical computing and graphics platform (v4.2.2 “Innocent and Trusting”).

In the analysis of wpVPM and ulVPM datasets (control and embWPC samples) generated for this study, significantly differentially expressed genes (DEGs) were identified using a simultaneous statistical significance threshold (Benjamini–Hochberg (BH) adjusted *P* value <0.1) and absolute log2 fold change (log2FC) >0.14 by shrunken log2FC using the adaptive *T* prior Bayesian shrinkage estimator “apeglm” (Supplementary Data 1, 2)<sup>66</sup>. Hierarchical clustering

analysis was performed using “Euclidean” distance and “Complete” clustering methods metrics to visualize significantly upregulated and downregulated genes. A linear support vector machine (SVM) model for classifying RNA-seq samples was developed using the e1071 package (v1.7-14). This model was based on the gene expression profiles of the top 500 most variable genes in ulVPM and wpVPM control samples. Subsequently, the C-SVM model was utilized to predict the classification of ulVPM-embWPC samples based on their transcriptomic profiles.

Functional enrichment analyses were performed using clusterProfiler (v4.4.4)<sup>67</sup> under org.Mm.eg.db package (v3.15) for better annotation data. All enriched terms were considered significant at adjusted *P* values by “BH” <0.1, in the Gene Ontology (GO) overrepresentation Analysis. Enrichment results were further clustered and simplified using the simplifyEnrichment package (version 1.11.1)<sup>68</sup> (Supplementary Data 3).

### Ex vivo calcium imaging

At E16, embryos were retrieved from the dam’s uterus by cesarean section, their brains were rapidly dissected out, and they were submerged in an ice-cold slicing solution containing (in mM): 2.5 KCl, 7 MgSO<sub>4</sub>, 0.5 CaCl<sub>2</sub>, 1 NaH<sub>2</sub>PO<sub>4</sub>, 26 Na<sub>2</sub>HCO<sub>3</sub>, 11 glucose, and 228 sucrose. Coronal slices (350-μm thick) were obtained using a vibratome (VT1200S Leica), and they were left to recover for at least 30 min at room temperature in standard artificial cerebrospinal fluid (ACSF) containing (in mM): 119 NaCl, 5 KCl, 1.3 MgSO<sub>4</sub>, 2.4 CaCl<sub>2</sub>, 1 NaH<sub>2</sub>PO<sub>4</sub>, 26 Na<sub>2</sub>HCO<sub>3</sub>, and 11 glucose. All extracellular solutions were continuously bubbled with a 95% O<sub>2</sub> and 5% CO<sub>2</sub> gas mixture. Slices were loaded with the calcium indicator Cal520TM (AAT Bioquest) as previously described<sup>10,21</sup>, transferred to a submersion-type recording chamber, and perfused with warm ACSF (32–34 °C) at a rate of 1.8 ml/min. Images were acquired with a digital charge-coupled device (CCD) camera (ORCA-R2 C10600-10B, Hamamatsu) coupled to an upright microscope (DM-LFSA, Leica) and using a 5x objective. For recordings of spontaneous calcium activity, frames were acquired with an exposure time of 150 ms, an interframe interval of 300 ms, a frame size of 672 × 512 pixel, and a spatial resolution of 2.5 μm/pixel. With each slice, 1 to 5 epochs of 15 min (3000 frames) were recorded.

### Analysis of fluorescence spontaneous activity

Analysis of spontaneous thalamic calcium activity was conducted using custom software developed in Matlab™, which was adapted from the CalciumDX toolbox (indexed in the Data and code availability section). For each movie, VPM was delineated, and the two prospective areas (wpVPM and ulVPM) were subdivided into a grid of 6 × 6 pixels where each small square is a region of interest (ROI). Calcium activity events were detected based on the average calcium signal of each ROI over time, employing threshold-based algorithms modified from CalciumDX. To identify significant synchronous activity and discard ROI co-activation that results from random temporal coincidence of calcium events, we generated surrogated calcium events sequences for each experiment using Matlab™. The alternative dataset was built by randomly shuffling the original temporal intervals between calcium transients in every ROI while preserving the spiking frequency and temporal structure of the calcium activity. Subsequently, the maximum value of co-activation from shuffled data was calculated. Through 1000 iterations, we established a synchronicity threshold as the 95th percentile of the maximum values of co-activation obtained from the shuffled dataset. In each experiment, only activity surpassing the synchronicity threshold was used for calculations and visualization. The onset of a synchronic event was defined as the frame in which co-activation overpassed the threshold, while the end was determined as the frame in which co-activation reached 25% of peak synchronicity.

### Behavioral testing

Twenty-three mice (9 males, 14 females) from four litters were bred for behavioral testing in adulthood (4 months old). Mice were housed in groups of 2–4 per cage. All behavioral testing was conducted during the light phase.

To evaluate tactile sensory processing, we used mice with bilateral (rather than unilateral) whisker pad cauterization at E14 (bi-embWPC group), enabling a more precise assessment of whisker-dependent processing by eliminating potential compensatory input in response to vibrissae-driven sensory stimuli from the intact contralateral side of the snout in unilateral cauterized mice. Wild-type littermates with intact whiskers served as control mice, while an additional control group of wild-type littermates underwent acute whisker trimming to assess texture discrimination in the absence of mystacial vibrissae input. Whisker trimming occurred on day 2, three hours after the second habituation session (see protocol below). All groups of mice were anesthetized with 5% isoflurane for induction and maintained on 2% isoflurane for 10 min. In the trimmed group, precise trimming to the fur level was achieved using micro spring scissors and a surgical microscope, carefully sparing upper lip whiskers.

Mice were habituated to handling and the testing room over 5–7 days, with dim lighting (20–30 lux) before testing. The behavioral testing arena was a black methacrylate box (40 × 40 × 40 cm) with no visual cues, and illumination was kept low (3–5 lux) to minimize visual information. Target objects consisted of 3D-printed cylinders (4 cm diameter, 9 cm height) covered with sandpaper of either 80 or 180 grit (P80 or P180) using double-sided tape. Six sets of textured covers were prepared a week prior to testing to minimize residual odors; each set contained four covers (three P180 and one P80), avoiding repetitive use and minimizing olfactory interference.

We used a modified whisker-dependent texture discrimination task based on established protocols<sup>69–71</sup>. This 3-day paradigm takes advantage of mice’s innate preference for novelty. During days 1 and 2 (habituation sessions), mice freely explored the empty arena for 5 min each day. On day 3 (testing sessions), two identical P180 sandpaper-covered cylinders were placed diagonally within the arena (12 cm from walls, 15 cm apart) during the sample session (t<sub>1</sub>). Mice explored these objects for 5 min before being returned to their home cages for a 2-min inter-trial interval (ITI). During this interval, the arena and objects were cleaned with 70% ethanol, one P180 cover was replaced with a P80 sandpaper to create a novel texture, and the other P180 cover was replaced by a new P180 cover. The short ITI minimized the influence of hippocampal processes on texture discrimination. During the test session (t<sub>2</sub>), mice were returned to the arena to explore both the familiar (P180) and novel (P80) textures for 5 min. Mice were acclimated to the testing room for 30–60 min prior to each session.

Data analyses were performed offline using custom Matlab scripts to track and analyze locomotor and exploratory behaviors. Texture discrimination was assessed using the discrimination index (DI), calculated as the proportion of time spent exploring the novel texture relative to the total exploration time, according to the formula:

$$DI = \frac{T_{new}}{T_{new} + T_{familiar}}$$

where  $T_{new}$  refers to the time spent exploring the novel texture (P80) and  $T_{familiar}$  is the time spent on the familiar texture (P180). In sample session (t<sub>1</sub>),  $T_{new}$  refers to the texture that will be replaced in the following test session (t<sub>2</sub>). DI values range from 0 to 1, with a value of 0.5 indicating no preference, and values above 0.5 indicating a preference for the novel texture.

### Statistical analysis

Data were analysed using Prism 9 (GraphPad). A Kolmogorov-Smirnov normality test was conducted on all datasets. For independent data

that conforms to a normal distribution, an unpaired two-tailed Student's *t*-test was employed to compare the two groups. In cases where independent data that did not follow a normal distribution, a Mann–Whitney *U*-test two-tailed test was used for comparison. For analyses involving more than two groups and one factor, one-way ANOVA was applied, followed by a Tukey post hoc analysis when data exhibited a normal distribution. For more than two groups and two factors, two-way ANOVA was conducted, followed by a Tukey post hoc analysis for normally distributed data. When data did not conform to a normal distribution, a Kruskal–Wallis test was performed, followed by Dunn's multiple comparisons without any correction. Results are presented as mean  $\pm$  standard error of mean (SEM) with the *n* value for each dataset. Statistically significant effects and *n* numbers are detailed in the corresponding figure legend or Methods. The significance threshold was set at 0.05, two-tailed (not significant, ns,  $p > 0.05$ ; \* $p < 0.05$ ; \*\* $p < 0.01$ ; \*\*\* $p < 0.001$ ). In the bioinformatical analysis, DEGs were identified using a statistical significance threshold (BH-adjusted *p* value  $< 0.1$ ) and set as follows: \*adj.  $p < 0.1$ , \*\*adj.  $p < 0.01$ , and \*\*\*adj.  $p < 0.001$ . No data exclusion was performed. Data for RNA-seq were processed according to the description in the Methods sections, and statistical details are explained in the results and corresponding figure legends.

## Quantifications

**Main figures.** In Fig. 1b: Whisker pad volume, unpaired two-tailed Student *t*-test. \*\* $p < 0.01$ . Upper lip volume, unpaired two-tailed Student *t*-test. ns,  $p = 0.11$ . Upper lip area, unpaired two-tailed Student *t*-test. ns,  $p = 0.32$ . 9 follicles volume, two-tailed Mann–Whitney *U*-test. \* $p < 0.05$ . ns,  $p = 0.73$ . Upper lip number of follicles, unpaired two-tailed Student *t*-test. ns,  $p = 0.78$ . In Fig. 1d: unpaired two-tailed Student *t*-test. PMBSF, \*\*\* $p < 0.0001$ , ALBSF, \*\*\* $p = 0.0002$ . In Fig. 1f: unpaired two-tailed Student *t*-test. Dil, \*\*\* $p = 0.0002$ , DiA, \*\*\* $p < 0.0001$ . In Fig. 1h: unpaired two-tailed Student *t*-test. ns, PMBSF,  $p = 0.55$ , ALBSF,  $p = 0.30$ . In Fig. 1j: unpaired two-tailed Student *t*-test. ns,  $p = 0.09$ . \*\* $p < 0.01$ .

In Fig. 2c: unpaired two-tailed Student *t*-test. PMBSF active fraction after wps, \* $p = 0.0198$ , PMBSF active fraction after uls, \*\*\* $p = 0.0001$ , ALBSF active fraction after wps, \*\* $p = 0.0037$ , ALBSF active fraction after uls, \*\* $p = 0.0014$ . In Fig. 2e: PMBSF active fraction, unpaired two-tailed Student *t*-test. \*\* $p < 0.01$ . ALBSF active fraction, two-tailed Mann–Whitney *U*-test. ns,  $p = 0.06$ . \* $p < 0.05$ . In Fig. 2f: Kruskal–Wallis test, \*\*\* $p < 0.001$ . Dunn's multiple comparison test post hoc analysis, ctrl E18 vs embWPC E18 ns,  $p = 0.37$ ; ctrl E18 vs ctrl P4, \*\*\* $p = 0.0009$ ; ctrl E18 vs embWPC P4, \*\*\* $p < 0.0001$ ; embWPC E18 vs ctrl P4 ns,  $p = 0.77$ ; embWPC E18 vs embWPC P4 ns,  $p = 0.14$ ; ctrl P4 vs embWPC P4 ns,  $p > 0.999$ .

In Fig. 3d: Kruskal–Wallis test, \*\*\* $p < 0.001$ . Dunn's multiple comparison test post hoc analysis, wpVPM-ctrl vs wpVPM embWPC ns,  $p = 0.14$ ; wpVPM-ctrl vs ulVPM-embWPC ns,  $p = 0.32$ ; wpVPM embWPC vs ulVPM-embWPC ns,  $p > 0.99$ . wpVPM-ctrl vs ulVPM-ctrl, \* $p = 0.04$ . ulVPM-ctrl vs ulVPM-embWPC, \*\*\* $p < 0.0001$ . In Fig. 3f: Thalamus, wpVPM, two-way ANOVA test: \*\*\* $p < 0.001$ . Tukey's multiple comparison test post hoc analysis, ns,  $p = 0.98$ . \*\*\* $p < 0.0001$ ; ulVPM, Kruskal–Wallis test, \*\*\* $p = 0.0005$ . Dunn's multiple comparison test post hoc analysis, ns,  $p > 0.99$ . \*\* $p = 0.0019$ . Cortex, PMBSF, two-way ANOVA test: \*\*\* $p < 0.0001$ . Tukey's multiple comparison test post hoc analysis, ns,  $p = 0.99$ . \*\*\* $p < 0.0001$ ; ALBSF, two-way ANOVA test: \*\*\* $p < 0.0001$ . Tukey's multiple comparison test post hoc analysis, ns,  $p = 0.52$ . \*\*\* $p = 0.0002$ . In Fig. 3h: Dil, two-tailed Mann–Whitney *U*-test. ns,  $p = 0.7$ ; DiA, unpaired two-tailed Student *t*-test. ns, 0.76.

In Fig. 4b: One-way ANOVA test: \*\*\* $p < 0.0001$ . Tukey's multiple comparison test post hoc analysis, ns,  $p = 0.056$ , \*\*\* $p < 0.0001$ . In Fig. 4i: Negative binomial generalized linear model (GLM) analysis, *p* values were calculated using a two-tailed Wald's test. Adjusted

*p* values were obtained using the Benjamini–Hochberg (BH) method for multiple comparisons, with a significance threshold of adjusted *p* value  $< 0.1$ . *Rora* wpVPM-ctrl vs ulVPM-ctrl, \*\*\*adj.  $p < 0.0001$ ; *Rora* wpVPM-ctrl vs ulVPM-embWPC ns, adj.  $p = 0.98$ ; *Rora* ulVPM-ctrl vs ulVPM-embWPC, \*\*adj.  $p = 0.002$ ; *Hs6st2* wpVPM-ctrl vs ulVPM-ctrl, \*\*\*adj.  $p < 0.0001$ ; *Hs6st2* wpVPM-ctrl vs ulVPM-embWPC, \*adj.  $p = 0.04$ ; *Hs6st2* ulVPM-ctrl vs ulVPM-embWPC, \*\*\*adj.  $p < 0.0001$ ; *Pou2f2* wpVPM-ctrl vs ulVPM-ctrl, \*\*\*adj.  $p < 0.0001$ ; *Pou2f2* wpVPM-ctrl vs ulVPM-embWPC, \*adj.  $p = 0.07$ ; *Pou2f2* ulVPM-ctrl vs ulVPM-embWPC, \*\*\*adj.  $p = 0.0003$ ; *Epha4* wpVPM-ctrl vs ulVPM-ctrl, \*\*\*adj.  $p = 0.0008$ ; *Epha4* wpVPM-ctrl vs ulVPM-embWPC ns, adj.  $p = 0.79$ ; *Epha4* ulVPM-ctrl vs ulVPM-embWPC, \*adj.  $p = 0.08$ ; *Plxna2* wpVPM-ctrl vs ulVPM-ctrl, \*\*\*adj.  $p < 0.0001$ ; *Plxna2* wpVPM-ctrl vs ulVPM-embWPC, \*adj.  $p = 0.06$ ; *Plxna2* ulVPM-ctrl vs ulVPM-embWPC, \*\*\*adj.  $p < 0.0001$ ; *Cdh9* wpVPM-ctrl vs ulVPM-ctrl, \*\*\*adj.  $p < 0.0001$ ; *Cdh9* wpVPM-ctrl vs ulVPM-embWPC ns, adj.  $p = 0.98$ ; *Cdh9* ulVPM-ctrl vs ulVPM-embWPC, \*\*\*adj.  $p < 0.0001$ .

In Fig. 5b: Barrels average area (34 barrels), Two-way ANOVA test: \*\*\* $p < 0.0001$ . Tukey's multiple comparison test post hoc analysis, ns,  $p = 0.88$ . \*\*\* $p < 0.0001$ . Average area of four barrels per three caudal-to-rostral levels, Two-way ANOVA test: \*\*\* $p < 0.0001$ . Tukey's multiple comparison test post hoc analysis, level 1 ALBSF-ctrl vs ALBSF-embWPC, \*\*\* $p < 0.0001$ ; level 2 ALBSF-ctrl vs ALBSF-embWPC, \*\*\* $p < 0.0001$ ; level 3 ALBSF-ctrl vs ALBSF-embWPC, ns,  $p = 0.21$ ; level 1 ALBSF-ctrl vs level 2 ALBSF-ctrl, ns,  $p > 0.99$ ; level 1 ALBSF-ctrl vs level 3 ALBSF-ctrl, ns,  $p = 0.88$ ; level 2 ALBSF-ctrl vs level 3 ALBSF-ctrl, ns,  $p = 0.92$ ; level 1 ALBSF-embWPC vs level 2 ALBSF-embWPC, \*\* $p = 0.0023$ ; level 1 ALBSF-embWPC vs level 3 ALBSF-embWPC, \*\*\* $p < 0.0001$ ; level 2 ALBSF-embWPC vs level 3 ALBSF-embWPC, \*\* $p = 0.0027$ . In Fig. 5c: barrel/septum fluorescence ratio ( $\Delta F_b/F_s$ ), Two-way ANOVA test: \*\*\* $p < 0.0001$ . Tukey's multiple comparison test post hoc analysis, PMBSF-ctrl vs ALBSF-embWPC ns,  $p = 0.80$ ; ALBSF-ctrl vs ALBSF-POWPC ns,  $p = 0.35$ ; PMBSF-ctrl vs ALBSF-ctrl, \*\*\* $p < 0.0001$ ; ALBSF-ctrl vs ALBSF-embWPC, \*\*\* $p < 0.0001$ ; PMBSF-ctrl vs ALBSF-POWPC, \*\*\* $p < 0.0001$ ; ALBSF-embWPC vs ALBSF-POWPC, \*\*\* $p < 0.0001$ . Gray value fluorescence intensity in a barrel, one-way ANOVA test: \*\*\* $p = 0.0002$ . Tukey's multiple comparison test post hoc analysis, ns,  $p = 0.99$ . PMBSF-ctrl vs ALBSF-embWPC ns,  $p = 0.99$ ; ALBSF-ctrl vs ALBSF-POWPC ns,  $p = 0.99$ ; ALBSF-ctrl vs ALBSF-embWPC, \* $p = 0.01$ ; PMBSF-ctrl vs ALBSF-ctrl, \*\* $p = 0.005$ ; ALBSF-embWPC vs ALBSF-POWPC, \*\* $p = 0.005$ ; PMBSF-ctrl vs ALBSF-POWPC, \*\* $p = 0.0023$ . In Fig. 5e: One-way ANOVA test: \* $p = 0.01$ . Tukey's multiple comparison test post hoc analysis, PMBSF-ctrl vs ALBSF-embWPC ns,  $p = 0.75$ ; ALBSF-ctrl vs PMBSF-ctrl, \* $p = 0.048$ ; ALBSF-ctrl vs ALBSF-embWPC, \* $p = 0.013$ . In Fig. 5g: PV+ cells in barrels P8, one-way ANOVA test: \*\*\* $p < 0.0001$ . Tukey's multiple comparison test post hoc analysis, PMBSF-ctrl vs ALBSF-embWPC ns,  $p = 0.98$ ; PMBSF-ctrl vs ALBSF-ctrl, \*\*\* $p = 0.0003$ ; ALBSF-embWPC vs ALBSF-ctrl, \*\*\* $p = 0.0002$ . PV+ cells in septa P8, one-way ANOVA test: \*\*\* $p < 0.0001$ . Tukey's multiple comparison test post hoc analysis, PMBSF-ctrl vs ALBSF-embWPC ns,  $p > 0.99$ ; PMBSF-ctrl vs ALBSF-ctrl, \*\*\* $p < 0.0001$ ; ALBSF-embWPC vs ALBSF-ctrl, \*\*\* $p < 0.0001$ .

In Fig. 6c: One-way ANOVA test: \*\*\* $p < 0.0001$ . Tukey's multiple comparison test post hoc analysis, ns,  $p = 0.18$ . \*\*\* $p < 0.0001$ . In Fig. 6f: PMBSF, unpaired two-tailed Student *t*-test. \*\*\* $p < 0.0001$ ; ALBSF, two-tailed Mann–Whitney *U*-test. \*\*\* $p = 0.0002$ . In Fig. 6j: Total time of exploration, Two-way ANOVA test: \*\* $p = 0.0023$ . Tukey's multiple comparison test post hoc analysis, t1 ctrl vs bi-embWPC, \* $p = 0.05$ ; t1 ctrl vs trimmed, \*\* $p = 0.001$ , t1 bi-embWPC vs trimmed ns,  $p = 0.42$ ; t2 ctrl vs bi-embWPC, \* $p = 0.029$ ; t2 ctrl vs trimmed, \* $p = 0.029$ , t2 bi-embWPC vs trimmed ns,  $p = 0.997$ . Discrimination Index, Two-way ANOVA test: \*\* $p = 0.002$ . Bonferroni's multiple comparison test post hoc test; t1 ctrl vs t2 ctrl, \* $p = 0.035$ ; t1 bi-embWPC vs t2 bi-embWPC, \*\* $p = 0.009$ ; t1 trimmed vs t2 trimmed ns,  $p > 0.999$ .



## Declaration of generative AI and AI-assisted technologies in the writing process

During the preparation of this work the authors used Chat-GPT in order to streamline some parts of the text. After using this tool, the authors reviewed and edited the content as needed and took full responsibility for the content of the publication.

## Reporting summary

Further information on research design is available in the Nature Portfolio Reporting Summary linked to this article.

## Data availability

RNAseq datasets have been deposited at the National Center for Biotechnology Information (NCBI) Gene Expression Omnibus (GEO) as GEO: [GSE260865](https://www.ncbi.nlm.nih.gov/geo/query/acc.cgi?acc=GSE260865) and are publicly available as of the date of publication. The remaining data were available within the Article, Supplementary Information, or Source data file. Any additional information required to reanalyze the data reported in this working paper is available from the lead contact upon request. Source data are provided with this paper.

## Code availability

This study did not generate the original code. For ex vivo experiments analysis, calcium imaging code previously reported<sup>21</sup> and deposited at <https://github.com/ackman678/CalciumDX>. For in vivo calcium imaging experiments, the code from WholeBrainDX repository<sup>61</sup> (available at <https://github.com/ackman678/wholeBrainDX>) was employed to prepare the supplementary videos. For behavioral experiments, video recordings were processed using custom codes developed with Matlab's Image Processing Toolbox.

## References

- Rakic, P. Specification of cerebral cortical areas. *Science* **241**, 170–176 (1988).
- O'Leary, D. D. & Sahara, S. Genetic regulation of arealization of the neocortex. *Curr. Opin. Neurobiol.* **18**, 90–100 (2008).
- O'Leary, D. D., Chou, S. J. & Sahara, S. Area patterning of the mammalian cortex. *Neuron* **56**, 252–269 (2007).
- Grove, E. A. & Fukuchi-Shimogori, T. Generating the cerebral cortical area map. *Annu. Rev. Neurosci.* **26**, 355–380 (2003).
- Harris, K. D. & Shepherd, G. M. The neocortical circuit: themes and variations. *Nat. Neurosci.* **18**, 170–181 (2015).
- Welker, C. Receptive fields of barrels in the somatosensory neocortex of the rat. *J. Comp. Neurol.* **166**, 173–189 (1976).
- Diamond, M. E., von Heimendahl, M., Knutsen, P. M., Kleinfeld, D. & Ahissar, E. Where' and 'what' in the whisker sensorimotor system. *Nat. Rev. Neurosci.* **9**, 601–612 (2008).
- Brecht, M., Preilowski, B. & Merzenich, M. M. Functional architecture of the mystacial vibrissae. *Behav. Brain Res.* **84**, 81–97 (1997).
- Woolsey, T. A. & Van der Loos, H. The structural organization of layer IV in the somatosensory region (SI) of mouse cerebral cortex. The description of a cortical field composed of discrete cytoarchitectonic units. *Brain Res.* **17**, 205–242 (1970).
- Moreno-Juan, V. et al. Prenatal thalamic waves regulate cortical area size prior to sensory processing. *Nat. Commun.* **8**, 14172 (2017).
- Lopez-Bendito, G., Anibal-Martinez, M. & Martini, F. J. Cross-modal plasticity in brains deprived of visual input before vision. *Annu. Rev. Neurosci.* **45**, 471–489 (2022).
- Gaspar, P. & Erzurumlu, R. The birth of the barrels. *Dev. Cell* **27**, 3–4 (2013).
- Erzurumlu, R. S. & Gaspar, P. How the barrel cortex became a working model for developmental plasticity: a historical perspective. *J. Neurosci.* **40**, 6460–6473 (2020).
- Mizuno, H. et al. NMDAR-regulated dynamics of layer 4 neuronal dendrites during thalamocortical reorganization in neonates. *Neuron* **82**, 365–379 (2014).
- Laumonerie, C. et al. Facial whisker pattern is not sufficient to instruct a whisker-related topographic map in the mouse somatosensory brainstem. *Development* **142**, 3704–3712 (2015).
- Ozdinler, P. H. & Erzurumlu, R. S. Slit2, a branching-arborization factor for sensory axons in the mammalian CNS. *J. Neurosci.* **22**, 4540–4549 (2002).
- Oury, F. et al. Hoxa2- and rhombomere-dependent development of the mouse facial somatosensory map. *Science* **313**, 1408–1413 (2006).
- Kitazawa, T. & Rijli, F. M. Barrelette map formation in the prenatal mouse brainstem. *Curr. Opin. Neurobiol.* **53**, 210–219 (2018).
- Bechara, A. et al. Hoxa2 selects barrelette neuron identity and connectivity in the mouse somatosensory brainstem. *Cell Rep.* **13**, 783–797 (2015).
- Zembrzycki, A., Chou, S. J., Ashery-Padan, R., Stoykova, A. & O'Leary, D. D. Sensory cortex limits cortical maps and drives top-down plasticity in thalamocortical circuits. *Nat. Neurosci.* **16**, 1060–1067 (2013).
- Anton-Bolanos, N. et al. Prenatal activity from thalamic neurons governs the emergence of functional cortical maps in mice. *Science* **364**, 987–990 (2019).
- Guillamon-Vivancos, T. et al. Input-dependent segregation of visual and somatosensory circuits in the mouse superior colliculus. *Science* **377**, 845–850 (2022).
- Frangeul, L. et al. A cross-modal genetic framework for the development and plasticity of sensory pathways. *Nature* **538**, 96–98 (2016).
- Pouchelon, G. et al. Modality-specific thalamocortical inputs instruct the identity of postsynaptic L4 neurons. *Nature* **511**, 471–474 (2014).
- Ono, K. et al. Development of the prethalamus is crucial for thalamocortical projection formation and is regulated by Olig2. *Development* **141**, 2075–2084 (2014).
- Vitalis, T. et al. RORalpha coordinates thalamic and cortical maturation to instruct barrel cortex development. *Cereb. Cortex* **28**, 3994–4007 (2018).
- Gezelius, H. & Lopez-Bendito, G. Thalamic neuronal specification and early circuit formation. *Dev. Neurobiol.* **77**, 830–843 (2017).
- Rubenstein, J. et al. Genetic control of cortical regionalization and connectivity. *Cereb. Cortex* **9**, 524–532 (1999).
- Mercurio, S. et al. Sox2 acts in thalamic neurons to control the development of retina-thalamus-cortex connectivity. *iScience* **15**, 257–273 (2019).
- Nakagawa, Y. & O'Leary, D. D. Dynamic patterned expression of orphan nuclear receptor genes RORalpha and RORbeta in developing mouse forebrain. *Dev. Neurosci.* **25**, 234–244 (2003).
- Yuge, K. et al. Region-specific gene expression in early postnatal mouse thalamus. *J. Comp. Neurol.* **519**, 544–561 (2011).
- Ebisu, H., Iwai-Takekoshi, L., Fujita-Jimbo, E., Momoi, T. & Kawasaki, H. Foxp2 regulates identities and projection patterns of thalamic nuclei during development. *Cereb. Cortex* **27**, 3648–3659 (2017).
- Puelles, L., Sanchez, M. P., Spreafico, R. & Fairen, A. Prenatal development of calbindin immunoreactivity in the dorsal thalamus of the rat. *Neuroscience* **46**, 135–147 (1992).
- Dufour, A. et al. Area specificity and topography of thalamocortical projections are controlled by ephrin/Eph genes. *Neuron* **39**, 453–465 (2003).
- Shigematsu, N., Miyamoto, Y., Esumi, S. & Fukuda, T. The anterolateral barrel subfield differs from the posteromedial barrel subfield in the morphology and cell density of parvalbumin-positive

- GABAergic interneurons. *eNeuro* <https://doi.org/10.1523/ENEURO.0518-22.2024> (2024).
36. Killackey, H. P. & Dawson, D. R. Expansion of the central hindpaw representation following fetal forelimb removal in the rat. *Eur. J. Neurosci.* **1**, 210–221 (1989).
  37. Van der Loos, H. & Woolsey, T. A. Somatosensory cortex: structural alterations following early injury to sense organs. *Science* **179**, 395–398 (1973).
  38. Killackey, H. P. & Belford, G. R. The formation of afferent patterns in the somatosensory cortex of the neonatal rat. *J. Comp. Neurol.* **183**, 285–303 (1979).
  39. Woolsey, T. A., Anderson, J. R., Wann, J. R. & Stanfield, B. B. Effects of early vibrissae damage on neurons in the ventrobasal (VB) thalamus of the mouse. *J. Comp. Neurol.* **184**, 363–380 (1979).
  40. Belford, G. R. & Killackey, H. P. The development of vibrissae representation in subcortical trigeminal centers of the neonatal rat. *J. Comp. Neurol.* **188**, 63–74 (1979).
  41. Woolsey, T. A. & Wann, J. R. Areal changes in mouse cortical barrels following vibrissal damage at different postnatal ages. *J. Comp. Neurol.* **170**, 53–66 (1976).
  42. Killackey, H. P., Belford, G., Ryugo, R. & Ryugo, D. K. Anomalous organization of thalamocortical projections consequent to vibrissae removal in the newborn rat and mouse. *Brain Res.* **104**, 309–315 (1976).
  43. Renier, N. et al. A mutant with bilateral whisker to barrel inputs unveils somatosensory mapping rules in the cerebral cortex. *Elife* <https://doi.org/10.7554/eLife.23494> (2017).
  44. Belford, G. R. & Killackey, H. P. The sensitive period in the development of the trigeminal system of the neonatal rat. *J. Comp. Neurol.* **193**, 335–350 (1980).
  45. Martini, F. J., Guillamon-Vivancos, T., Moreno-Juan, V., Valdeolmillos, M. & Lopez-Bendito, G. Spontaneous activity in developing thalamic and cortical sensory networks. *Neuron* **109**, 2519–2534 (2021).
  46. Mire, E. et al. Spontaneous activity regulates Robo1 transcription to mediate a switch in thalamocortical axon growth. *Nat. Neurosci.* **15**, 1134–1143 (2012).
  47. Land, P. W. & Simons, D. J. Cytochrome oxidase staining in the rat Sml barrel cortex. *J. Comp. Neurol.* **238**, 225–235 (1985).
  48. Jan, T. A., Lu, L., Li, C. X., Williams, R. W. & Waters, R. S. Genetic analysis of posterior medial barrel subfield (PMBSF) size in somatosensory cortex (SI) in recombinant inbred strains of mice. *BMC Neurosci.* **9**, 3 (2008).
  49. Kleinfeld, D., Ahissar, E. & Diamond, M. E. Active sensation: insights from the rodent vibrissa sensorimotor system. *Curr. Opin. Neurobiol.* **16**, 435–444 (2006).
  50. Grant, R. A., Sperber, A. L. & Prescott, T. J. The role of orienting in vibrissal touch sensing. *Front. Behav. Neurosci.* **6**, 39 (2012).
  51. Kuruppath, P., Gugig, E. & Azouz, R. Microvibrissae-based texture discrimination. *J. Neurosci.* **34**, 5115–5120 (2014).
  52. Morita, T., Kang, H., Wolfe, J., Jadhav, S. P. & Feldman, D. E. Psychometric curve and behavioral strategies for whisker-based texture discrimination in rats. *PLoS ONE* **6**, e20437 (2011).
  53. Gorski, J. A. et al. Cortical excitatory neurons and glia, but not GABAergic neurons, are produced in the Emx1-expressing lineage. *J. Neurosci.* **22**, 6309–6314 (2002).
  54. Chen, L., Guo, Q. & Li, J. Transcription factor Gbx2 acts cell-nonautonomously to regulate the formation of lineage-restriction boundaries of the thalamus. *Development* **136**, 1317–1326 (2009).
  55. Franco, S. J. et al. Fate-restricted neural progenitors in the mammalian cerebral cortex. *Science* **337**, 746–749 (2012).
  56. Voiculescu, O., Charnay, P. & Schneider-Maunoury, S. Expression pattern of a Krox-20/Cre knock-in allele in the developing hind-brain, bones, and peripheral nervous system. *Genesis* **26**, 123–126 (2000).
  57. Madisen, L. et al. Transgenic mice for intersectional targeting of neural sensors and effectors with high specificity and performance. *Neuron* **85**, 942–958 (2015).
  58. Renier, N. et al. iDISCO: a simple, rapid method to immunolabel large tissue samples for volume imaging. *Cell* **159**, 896–910 (2014).
  59. Renier, N. et al. Mapping of brain activity by automated volume analysis of immediate early genes. *Cell* **165**, 1789–1802 (2016).
  60. Madisen, L. et al. A robust and high-throughput Cre reporting and characterization system for the whole mouse brain. *Nat. Neurosci.* **13**, 133–140 (2010).
  61. Ackman, J. B., Zeng, H. & Crair, M. C. Structured dynamics of neural activity across developing neocortex. Preprint at *bioRxiv* <https://doi.org/10.1101/012237> (2014).
  62. Herrero-Navarro, A. et al. Astrocytes and neurons share region-specific transcriptional signatures that confer regional identity to neuronal reprogramming. *Sci. Adv.* <https://doi.org/10.1126/sciadv.abe8978> (2021).
  63. Dobin, A. et al. STAR: ultrafast universal RNA-seq aligner. *Bioinformatics* **29**, 15–21 (2013).
  64. Love, M. I., Huber, W. & Anders, S. Moderated estimation of fold change and dispersion for RNA-seq data with DESeq2. *Genome Biol.* **15**, 550 (2014).
  65. Huber, W. et al. Orchestrating high-throughput genomic analysis with Bioconductor. *Nat. Methods* **12**, 115–121 (2015).
  66. Zhu, A., Srivastava, A., Ibrahim, J. G., Patro, R. & Love, M. I. Non-parametric expression analysis using inferential replicate counts. *Nucleic Acids Res.* **47**, e105 (2019).
  67. Gu, Z. & Hubschmann, D. simplifyEnrichment: a bioconductor package for clustering and visualizing functional enrichment results. *Genomics Proteomics Bioinformatics* **21**, 190–202 (2023).
  68. Yu, G., Wang, L. G., Han, Y. & He, Q. Y. clusterProfiler: an R package for comparing biological themes among gene clusters. *OMICS* **16**, 284–287 (2012).
  69. Wu, H. P., Ioffe, J. C., Iverson, M. M., Boon, J. M. & Dyck, R. H. Novel, whisker-dependent texture discrimination task for mice. *Behav. Brain Res.* **237**, 238–242 (2013).
  70. Benamer, N., Vidal, M., Balia, M. & Angulo, M. C. Myelination of parvalbumin interneurons shapes the function of cortical sensory inhibitory circuits. *Nat. Commun.* **11**, 5151 (2020).
  71. Balasco, L. et al. Somatosensory cortex hyperconnectivity and impaired whisker-dependent responses in Cntnap2(-/-) mice. *Neurobiol. Dis.* **169**, 105742 (2022).

## Acknowledgements

We thank Belén Andrés and María Aurelia Torregrosa for their technical support. We thank Teresa Guillamón-Vivancos and Miguel Valdeolmillos for their comments and input on the manuscript and other members of López-Bendito's laboratory for stimulating discussions. This work was supported by grants from the Swiss National Science Foundation (31003A\_175776 and 310030\_219370) and the Novartis Research Foundation to F.M.R., and by grants from the European Research Council (ERC) under the European Union's Horizon 2020 research and innovation program (ERC-2021-ADG-101054313 SPONTSENSE), PID2021-127112NB-I00 from the MCIN/AEI/10.13039/501100011033/ and ERDF A way to make Europe, and Generalitat Valenciana, Conselleria d'Educació, Universitats, i Ocupació (PROMETEO 2021/052) to G.L.-B. This work was also funded by the Spanish State Research Agency (AEI/10.13039/501100011033), through the 'Severo Ochoa' Center of Excellence grant to the IN (CEX2021-001165-S).

## Author contributions

Conceptualization, M.A.-M. and G.L.-B.; methodology, M.A.-M., E.P.-M., G.P., M.P.M. and L.M.R.-M.; data curation, M.A.-M., E.P.-M., G.P., M.P.M., and L.P.; transcriptomic analysis, L.P.; writing—original draft, M.A.-M., and G.L.-B.; writing—review & editing, M.A.-M., L.P., E.P.-M., G.P., F.J.M.,

F.M.R., and G.L.-B.; funding acquisition, FM.R., and G.L.-B.; resources, FM.R., and G.L.-B.; supervision, F.J.M., FM.R., and G.L.-B.

## Competing interests

The authors declare no competing interests.

## Additional information

**Supplementary information** The online version contains supplementary material available at <https://doi.org/10.1038/s41467-025-57052-w>.

**Correspondence** and requests for materials should be addressed to Guillermina López-Bendito.

**Peer review information** *Nature Communications* thanks Leena Ibrahim who co-reviewed with Mansour Alyahyay, and the other, anonymous, reviewers for their contribution to the peer review of this work. A peer review file is available.

**Reprints and permissions information** is available at <http://www.nature.com/reprints>

**Publisher's note** Springer Nature remains neutral with regard to jurisdictional claims in published maps and institutional affiliations.

**Open Access** This article is licensed under a Creative Commons Attribution-NonCommercial-NoDerivatives 4.0 International License, which permits any non-commercial use, sharing, distribution and reproduction in any medium or format, as long as you give appropriate credit to the original author(s) and the source, provide a link to the Creative Commons licence, and indicate if you modified the licensed material. You do not have permission under this licence to share adapted material derived from this article or parts of it. The images or other third party material in this article are included in the article's Creative Commons licence, unless indicated otherwise in a credit line to the material. If material is not included in the article's Creative Commons licence and your intended use is not permitted by statutory regulation or exceeds the permitted use, you will need to obtain permission directly from the copyright holder. To view a copy of this licence, visit <http://creativecommons.org/licenses/by-nc-nd/4.0/>.

© The Author(s) 2025